1	Image-based machine learning for monitoring the dynamics of
2	deltaic islands in the Atchafalaya River Delta Complex
3	between 1991 and 2019
4	Jiangjie Yang <sup>1</sup> , Zhijun Dai <sup>1, 2*</sup> , Yaying Lou <sup>1</sup> , Xuefei Mei <sup>1</sup> , Fagherazzi Sergio <sup>3</sup>
5	1. State Key Laboratory of Estuarine and Coastal Research, East China Normal
6	University, Shanghai 200062, China
7	2. Laboratory for Marine Geology, Qingdao National Laboratory for Marine Science
8	and Technology, Qingdao, 266061, China
9	3. Department of Earth and Environment, Boston University, USA
10	
11	Highlight:
12	1. The deltaic islands in the Atchafalaya River Delta Complex demonstrate seaward
13	prograding characteristics.
14	2. Fluvial suspended sediment discharge and peak flow events are responsible for
15	morphodynamic changes of deltaic island in the Wax Lake Delta.
16	3. Dredge and sediment disposal are the significant factor in promoting the growth of
17	deltaic island in the Atchafalaya Delta.
18	4. Sea level rise at 8.17 mm/yr was unlikely to pose a threat to Wax Lake Delta, but
19	may submerge the Atchafalaya Delta 's eastern coast.
20	
21	Abstract:
22	Deltaic islands are distinct hydro-environmental zones with global significance in
23	food security, biodiversity conservation, and fishery industry. These islands are the

fundamental building blocks in many river deltas. However, deltaic islands are facing severe challenges due to the interference of intensive anthropogenic activities, sea level rise, and climate change. Here, dynamic changes of deltaic islands in Wax Lake Delta (WLD) and Atchafalaya Delta (AD), part of the Atchafalaya River Delta Complex (ARDC) in Louisiana, USA, were diagnosed based on remote sensing images from 1991 to 2019 through machine learning method. Results indicate a significant increase in the deltaic islands area of the ARDC at a rate of 1.29 km<sup>2</sup>/yr, with local expansion rates of .60 km<sup>2</sup>/yr for WLD and 0.69 km<sup>2</sup>/yr for AD. Meanwhile, all three parts of WLD naturally prograded seawards, with the western part (WP) and central part (CP) expanding southwestward to the sea, while the eastern part (EP) prograding southeastwards. Different from WLD, the three parts of AD irregularly expanded seawards under the impacts of anthropogenic activities. The WP and CP respectively expanded northwestwards and southwestwards, while the EP basically kept stable. Moreover, there are different drivers that dominate the growth of deltaic islands of WLD and AD. Specifically, fluvial suspended sediment discharge and peak flow events should be responsible for the shift in the spatial evolution of WLD, while dredging and sediment disposal contributed to the expansion of AD. Nevertheless, hurricanes and storms with different categories and landing locations caused short-term deltaic island erosion/sedimentation. Hurricanes and tropical storm events mainly generated erosive impacts on the deltaic islands of the WLD, while causing transient erosion or siltation on the deltaic islands of the AD. In addition, high-intensity hurricanes that make landfall east of the deltaic island caused more erosion in the AD. Furthermore, SLR, at

24

25

26

27

28

29

30

31

32

33

34

35

36

37

38

39

40

41

42

43

44

- 46 the current rate of 8.17 mm/yr, will not pose a threat to the deltaic island of WLD, while
- 47 eastern AD may have the risk of drowning. This study recognizes the complexity of
- 48 factors influencing the growth of deltaic islands, suggesting the knowledge is of critical
- 49 implications for the restoration and sustainable management of the Mississippi River
- Delta and other deltas around the world.
- 51 Keywords: Morphodynamics; Deltaic islands; Atchafalaya River Delta Complex;
- 52 Machine learning

53

#### 1. Introduction

- Deltaic islands, which form at the mouth of distributary channels, are the
- fundamental building blocks that create deltaic land in many river deltas (Shaw et al.,
- 56 2014; Nardin et al., 2016; Sendrowski et al., 2016). These islands are active and
- 57 vulnerable hydro-environmental zones with regional significance in terms of
- 58 biodiversity, conservation, and coastal community protection (Costanza et al., 2008;
- 59 Fagherazzi et al., 2015). However, deltaic islands are facing severe challenges around
- 60 the world because of a dramatic reduction in riverine sediment transport, sea level rise
- 61 (SLR), and storm erosion (Syvitski et al., 2009; Nienhuis et al., 2020; Dai et al., 2013,
- 62 2021). As a result, deltaic islands morphodynamics and associated disturbances by
- 63 natural and anthropogenic drivers have attracted worldwide attention in recent years
- 64 (Ericson et al., 2006; Syvitski et al., 2009; Fagherazzi et al., 2015; Nardin et al., 2016).
- Deltaic islands are formed by continuous deposition and vertical accretion of a
- mouth bar, and can efficiently contribute to the expansion of fluvial deltas thus restoring
- 67 coastal regions (Fagherazzi et al., 2015; Nardin et al., 2016; Zhou et al., 2020).

Fagherazzi et al. (2015) found that initially, mouth bars form by sedimentation associated with turbulent jet expansion. Nardin et al. (2016) discovered that deposition on emergent deltaic islands is influenced by vegetation, and that intermediate vegetation height and density may increase sedimentation and provide a stabilizing cover that creates more resilient deltas. In addition, many studies indicate that the decrease in riverine sediment, saltwater intrusion, intensified storm surge activities, and sea level rise have a significant impact on evolution of river mouth bars, thus affecting the development of deltaic islands (Reeve and Karunarathna, 2009; Syvitski et al., 2009; Dai et al., 2013; Anthony et al., 2015). Reeve and Karunarathna (2009) suggested that mouth bars would remain in a stable state if there is an abundant source of sediment from the external environment during sea level rise. Meanwhile, Syvitski et al. (2009) noted that sediment reduction by dam construction cause erosion of the delta front. Anthony et al. (2015) observed that dam construction, commercial sand mining and groundwater extraction increased the vulnerability of the Mekong mouth bar area; and that over 300 km of the Mekong delta coastline suffered strong erosion. Dai et al. (2021) noticed that the mouth bar in the Changjiang Estuary is still present, despite the reduction of fluvial sediment supply caused by the impoundment of the Three Gorges Dam. There is therefore a need to quantify the morphodynamic evolution of deltaic island and identify the drivers responsible for their changes. Herein we analyze the variations in deltaic island area in the Atchafalaya River Delta Complex (ARDC) based on a machine learning method applied to the Google Earth Engine cloud computer platform.

68

69

70

71

72

73

74

75

76

77

78

79

80

81

82

83

84

85

86

87

88

The ARDC is a combination of Wax Lake Delta (WLD) and Atchafalaya Delta (AD), in Louisiana. The deltaic islands of both WLD and AD are prograding seaward (Rosen and Xu, 2013). The Atchafalaya River delivers water and sediment from the Mississippi River and Red River into the Gulf of Mexico (Horowitz, 2010). It has formed two sub-deltas through the manmade Wax Lake outlet channel and the natural Atchafalaya River main channel since the 1950s (Shlemon, 1975). After the early 1970s floods, the subaqueous portion of both deltas developed into the WLD and AD (Roberts et al., 1980). Rosen and Xu (2013), using Landsat images at ~5-year intervals, found that the deltaic islands of ARDC prograded seaward in recent decades despite a decrease in sediment discharge. Shaw et al. (2014) estimated that the growth rate of the total area of subaqueous delta in WLD is 1.83 km<sup>2</sup>/yr between 1974 and 2016. Carle et al. (2015) found a net growth of 6.5 km<sup>2</sup> in the deltaic island of WLD after the historic flood of 2011 and observed that the vegetation community exhibits a sharp vegetation zonation along the elevation gradient of the deltaic islands. Bevington et al. (2017) investigated the relative contribution of river flooding, hurricanes, and cold fronts on elevation change in the prograding deltaic island of WLD and suggested that river flood caused the highest deltaic wetland sediment retention. Olliver et al (2020) showed that areally averaged vertical accretion increases from 0.33 to 2 cm per 60-day as riverine flood magnitude increases in WLD. Elliton et al. (2020) found that interactions between physical and biophysical processes regulate sediment transport in the deltaic island of WLD. In summary, previous works have paid considerable attention to the dynamics of WLD (Bevington et al., 2017; Carle et al., 2015; Elliton et al., 2020), but little

90

91

92

93

94

95

96

97

98

99

100

101

102

103

104

105

106

107

108

109

110

information is available for AD. Moreover, some studies observed that hurricanes may cause either degradation by transporting sediment away from deltaic islands, or siltation by delivering coastal sediment (Walker, 2001; Barras, 2007). However, the short-term impact of floods, hurricanes, and other storm events on deltaic islands is difficult to capture by sparse data remote sensing data at ~5-year intervals (Rosen and Xu, 2013). Therefore, it is essential to comprehensively understand the ARDC's morphodynamic response to external forcing using high temporal resolution and long-term datasets. Most studies on the dynamics of deltaic islands were based on field observations (DeLaune et al. 2016; Bevington et al., 2017; Elliton et al., 2020). Some models, including the hydrodynamic model (Nardin et al., 2016; Pertiwi et al., 2021) and morphological models (Fitzgerald, 1998; Roberts et al., 2003), were also introduced to analyze temporal and spatial changes in deltaic islands. However, these methods are time-consuming and laborious, and are difficult to carry out on a large scale to analyze temporal and spatial dynamics of deltaic islands. In recent years, remote sensing images have been used to monitor morphodynamics of deltaic islands (Rosen and Xu, 2013; Zhang et al., 2021). Google Earth Engine (GEE), a cloud computing platform able to quickly process millions of images (Gorelick et al., 2017; Zhang et al., 2022), has successfully produced annual maps of tidal flats (Wang et al., 2020), forests (Chen et al., 2017), mangroves (Long et al., 2021, 2022) and open water bodies (Zou et al., 2017). GEE provides many machine learning algorithms that are effectively utilized to extract land use type (Farad, 2017), explore groundwater arsenic distribution (Fu et al., 2022), discern mangrove dynamic processes (Long et al., 2021,2022), and estimate

112

113

114

115

116

117

118

119

120

121

122

123

124

125

126

127

128

129

130

131

132

water quality (Guo et al., 2021). Random Forest (RF), a non-parametric machine learning algorithm, has been used to classify spectral characteristics of different landforms. Magidi et al. (2021) applied the RF algorithm to distinguish irrigated and rainfed areas for Mpumalanga Province in Africa. Long et al. (2021) used the RF algorithm to discriminate tidal flats, mangroves and water bodies in the Nanliu River Delta. Lou et al. (2022) utilized the RF algorithm to classified open water, salt marshes and mudflats in the Changjiang River Delta. In this study, we aim to explore spatio-temporal dynamics of the deltaic island in ARDC from 1991 to 2019 using time series of Landsat images and the RF algorithm through the GEE platform. The specific objectives are to detect morphodynamic variations of deltaic islands in the ARDC and to diagnose the main drivers that can be responsible for these variations. This study could provide critical insight for the restoration and sustainable management of deltaic islands in the Mississippi River Delta and in other deltas around the world.

## 2 Materials and methods

#### 2.1 Study area

The Mississippi River is the fourth longest river in the world, starting from the source of the Missouri river, the largest tributary in the Rocky Mountains, with a length of 6262 km. The basin covers an area of 3.23 million km², about 1/4 of the area of America (Xu, 2010). Nowadays, the Mississippi River carries a flow of about 380 km³/yr and transports a sediment load of about 180 million tons to the Gulf of Mexico (Yang et al., 2021). As much as 10000 to 13000 km² of the Mississippi River Delta may

be lost or submerged because of SLR and subsidence by 2100 (Olson and Suski, 2021). Given the low wave energy and limited tidal range relative to the river discharge, the Mississippi River Delta is considered as a fluvial-dominated system (Keim et al., 2007; Bevington et al., 2017). The Mississippi River Delta was shaped by river flooding, tropical cyclones, and a predominantly east-to-west longshore current (Bevington et al., 2017). The Atchafalaya River (AR) is the largest tributary of the lower Mississippi River, with a length of about 190 km, and can capture about 30% of the Mississippi River discharge at the Old River Control Structure (ORCS) and the entire flow of the Red River (Horowitz, 2010). This water enters the Gulf of Mexico through the Wax Lake outlet channel and Atchafalaya River main channel, and forms deltaic islands in the WLD and AD, respectively (Fig. 1A; Horowitz, 2010; Xu and Bryantmason, 2011). The ORCS was built in 1963 to prevent the avulsion of the Mississippi River into the channel of the Atchafalaya River (Horowitz, 2010). Fluvial water and sediment discharge entering the Gulf of Mexico have obvious seasonal variations, with annual river floods occurring in spring (Mossa and Roberts, 1990). Both WLD and AD encompass several deltaic islands dominated by Sagittaria, Salix nigra, Typha, Polygonum, Nelumbo, and Phragmites australis (Rosen and Xu, 2013; Carle et al., 2015). Impacted by different hydrodynamic forcing, the deltaic islands of WLD and AD are both divided into three parts: the western part (WP), the central part (CP), and the eastern part (EP) respectively with their own distinct regional features as there are significant differences in sediment transport (Fig. 1C-D). Specifically, the CP is directly

155

156

157

158

159

160

161

162

163

164

165

166

167

168

169

170

171

172

173

174

175

exposed to fluvial action, while the WP and EP are relatively less affected by fluvial runoff.

## 2.2 Materials

In this study, a total of 262 remote sensing images from Landsat 5 TM (1991-2011), Landsat 7 ETM (2002-2003) and Landsat 8 OLI (2011-2019) are used to analyze the morphodynamic variations of the deltaic island in the ARDC (United States Geological Survey, USGS, https://earthexplorer.usgs.gov). Yearly tide level data from 1991 to 2019 at Grand Isle station and USGS Atchafalaya 2 Lidar data were downloaded from the National Oceanic and Atmospheric Administration (NOAA) (https://www.noaa.gov). Landsat images from June to September at similar low water level at Grand Isle were selected to minimize the impact of tidal levels and seasons on the delta evolution analysis (Table 1, 2).

Table 1 Deltaic island area in the WLD corresponding to tide level at Grand Isle station,
Overall accuracy and Kappa coefficient

Image time	Tide level (m)	Area (km²)	Overall accuracy	Kappa coefficient
1991-06-20	0.00	21.90	0.957	0.913
1992-09-10	0.35	15.02	0.956	0.963
1993-06-09	0.29	23.48	0.975	0.949
1994-08-15	0.22	22.27	0.967	0.986
1995-09-03	0.18	28.30	0.980	0.961
1996-07-03	0.16	30.67	0.942	0.933
1997-09-08	0.12	27.96	0.985	0.969
1998-07-09	0.18	28.70	0.933	0.942
1999-09-14	0.16	27.88	0.998	0.997
2000-09-16	0.16	29.97	0.965	0.921
2001-09-27	0.17	27.19	0.994	0.987
2002-08-05	0.25	24.06	0.958	0.932
2003-07-07	0.16	25.04	0.974	0.948
2004-07-25	0.14	28.14	0.976	0.925
2005-08-13	0.08	30.72	0.965	0.930
2006-09-01	0.16	24.22	0.992	0.899
2007-09-20	0.13	26.11	0.985	0.969
2008-09-22	0.23	26.59	0.932	0.973
2009-08-24	0.19	25.87	0.939	0.878
2010-09-28	0.09	29.85	0.925	0.913
2011-08-30	0.17	38.00	0.990	0.979
2013-06-16	0.16	37.30	0.943	0.925
2014-09-23	0.32	36.48	0.955	0.965
2015-07-08	0.16	43.68	0.989	0.979
2016-09-28	0.35	34.50	0.980	0.933
2017-09-15	0.20	39.59	0.935	0.912
2018-09-18	0.28	36.85	0.966	0.924
2019-09-05	0.15	38.78	0.985	0.970

Table 2 Deltaic island area in the AD corresponding to tide level at Grand Isle station, Overall accuracy and Kappa coefficient

Image time	Tide level (m)	Area (km²)	Overall accuracy	Kappa coefficient
1991-06-20	0.00	23.17	0.981	0.962
1992-09-10	0.35	24.88	0.926	0.986
1993-06-09	0.29	30.75	0.953	0.968
1994-08-15	0.22	33.71	0.968	0.988
1995-09-03	0.18	36.22	0.991	0.983
1996-07-03	0.16	41.95	0.986	0.987
1997-09-08	0.12	39.88	0.975	0.988
1998-07-09	0.18	48.25	0.977	0.986
1999-09-14	0.16	41.95	0.991	0.982
2000-09-16	0.16	37.25	0.956	0.976
2001-09-27	0.17	42.91	0.965	0.985
2002-08-05	0.25	35.19	0.958	0.966
2003-07-07	0.16	36.51	0.993	0.987
2004-07-25	0.14	44.63	0.986	0.954
2005-08-13	0.08	46.30	0.976	0.966
2006-09-01	0.16	42.09	0.972	0.986
2007-09-20	0.13	41.35	0.995	0.989
2008-09-22	0.23	38.10	0.983	0.989
2009-08-24	0.19	43.03	0.965	0.978
2010-09-28	0.09	47.74	0.968	0.987
2011-08-30	0.17	49.55	0.994	0.989
2013-06-16	0.16	48.40	0.942	0.986
2014-09-23	0.32	50.39	0.969	0.983
2015-07-08	0.16	51.79	0.992	0.985
2016-09-28	0.35	45.95	0.983	0.985
2017-09-15	0.20	43.22	0.953	0.966
2018-09-18	0.28	48.09	0.965	0.985
2019-09-05	0.15	51.68	0.994	0.987

Daily mean water discharge and annual suspended sediment discharge (SSD) at Wax Lake Outlet near Calumet (WLO) and Morgan City, Louisiana (MC) were collected from USGS (https://waterdata.usgs.gov/nwis). These data record the water flow and SSD through the Wax Lake outlet channel and Atchafalaya River main channel from 1991 to 2019. The annual water discharge for each year is counted by the sum of daily discharge within a year. In addition, information about hurricanes and

storm events occurring within 500 km from the ARDC center in the period 1991-2019 was collected from NOAA (Table 3). The surface elevation measured at the CRMS0479 in the WLD for the period of 2009/2/19-2021/3/8 and at the CRMS6304 in the AD for the period of 2009/10/19-2021/1/28 were collected from Coastwide Reference Monitoring System (https://www.lacoast.gov/crms/), which were instrumented with Rod Surface Elevation Tables.

Table 3 Hurricane and storm events attacked the ARDC during 1991-2019 corresponding with erosion/deposition by hurricanes and storms

Name	Year	Category	Distance (km)	Direction	Max wind speed (km/h)	Area change of the WLD	Area change of the AD
Andrew	1992	3	20	W	185.2	-3.86	1.56
Opal	1995	3	408	E	203.72	-2.35	-5.36
Josephine	1996	TS	184	E	111.12	-2.02	2.72
Danny	1997	1	85	E	129.64	0.35	2.54
Georges	1998	2	286	E	166.68	-2.33	0.23
Allison	2001	TS	19	W	92.6	-3.46	-0.96
Isidore	2002	TS	120	E	101.86		
Lili	2002	1	63	W	148.16	-5.34	-6.98
Matthew	2004	TS	70	E	74.08	0.43	2.23
Katrina	2005	3	180	E	203.72	-4.88	-3.11
Rita	2005	3	120	W	185.2	2.33	-0.28
Humberto	2007	1	246	W	148.16	-0.76	-1.01
Gustav	2008	2	70	Е	166.68	-1.78	-6.56
Ike	2008	2	324	W	175.94		
Isaac	2012	TS	134	Е	111.12		
Cindy	2017	TS	218	E	83.34	-8.47	2.89
Harvey	2017	TS	205	W	74.08	-6.08	-0.50
Nate	2017	1	218	Е	138.9	3.50	-2.63
Gordon	2018	TS	200	Е	111.12	-3.96	-0.80
Barry	2019	1	75	W	120.38	-5.38	0.81

\*Category is the Saffir-Simpson scale and identifies the wind strength of the storm at landfall. TS = Tropical storm, 63-118 km  $h^{-1}$ ; category 1 = 119-153 km  $h^{-1}$ ; category 2 = 154-177 km  $h^{-1}$ , Category 3 = 178-208 km  $h^{-1}$  (Rosen and Xu, 2013). Distance refers to the distance of hurricane and tropical storm from the ARDC center (Fig.1).

#### 2. 3 Methods

## 2.3.1 Methodological framework

The methodological framework describes the processes to classify deltaic islands and open water in the ARDC through machine learning algorithm based on the GEE platform (Fig. 2A; Lou et al., 2022). The procedure to classify deltaic island and open water followed four main stages: (1) training samples, (2) feature extraction, (3) separate deltaic island from the open water using spectral indices, and (4) vectorization and edge lines extraction (Fig. 2A). Note that the white lands that appeared suddenly on the Landsat images and distinctly different from the surrounding vegetated deltaic land and seawater were recognized as new land generated by dredge and spoil (Zhang et al., 2021). These white zones were outlined manually for further analysis.

## Training and validation samples

In order to investigate the evolution of the deltaic islands, we divided the ARDC into two categories - deltaic island and open water - through a process of manual visual interpretation of high-resolution images from Google Earth. Firstly, two layers were constructed and were respectively assigning each layer a class label (deltaic islands and open water); then, dozens of training polygons were manually selected and 1500 random points were generated by the 'random Point' command in GEE. Among them, 70% were set as training samples and the rest 30% were set as validation samples.

#### Spectral indices calculation

The pixel-based supervised RF algorithm effectively classify spectral characteristics of different landforms and discriminate deltaic islands from open water

according to four spectral indices: Nominalized Difference Vegetation Index (NDVI)

232 (Rouse et al., 1974), Enhanced Vegetation Index (EVI) (Huete et al., 2002), Land

Surface Water Index (LSWI) (Xiao et al., 2004) and modified Normalized Difference

234 Water Index (mNDWI) (Xu, 2006):

$$NDVI = \frac{\rho_{NIR} - \rho_{RED}}{\rho_{NIR} + \rho_{RED}} \tag{1}$$

$$EVI = 2.5 \times \frac{\rho_{NIR} - \rho_{RED}}{\rho_{NIR} + 6\rho_{RED} - 7\rho_{BLUE} + 1}$$
 (2)

$$LSWI = \frac{\rho_{NIR} - \rho_{SWIR}}{\rho_{NIR} + \rho_{SWIR}} \tag{3}$$

$$mNDWI = \frac{\rho_{GREEN} - \rho_{SWIR}}{\rho_{GREEN} + \rho_{SWIR}} \tag{4}$$

Where  $\rho_{BLUE}$ ,  $\rho_{GREEN}$ ,  $\rho_{RED}$ ,  $\rho_{NIR}$ ,  $\rho_{SWIR}$  are the blue, green, red, near-infrared,

and shortwave infrared bands of Landsat images, respectively. The value of these

spectral indices was extracted for each pixel in the training dataset.

#### Random Forest Classification

240

241

242

243

244

245

246

247

248

249

250

251

252

RF classifier uses a set of decision trees to predict classification or regression with the advantages of high precision, efficiency, and stability (Belgiu and Dr agu,t, 2016). This ensemble classifier has been widely used in remote sensing data for land cover classification (Lou et al., 2022; Bwangoy et al., 2010). GEE has programmed RF algorithm on their API which uses machine learning to classify available satellite images. Here, ee.Classifier.randomForest() function within the GEE platform was utilized for training a random forest classifier, using the extracted spectral indices and their corresponding class labels as input datasets. Ultimately, the entire image was classified by utilizing the trained random forest classifier, which was applied to the

spectral index values, resulting in the production of a classification map.

#### Accuracy assessment

Error analysis is necessary to verify the accuracy of the remote sensing resolution and images processing (Lawrence and Wright, 2001). For a better interpretation and correct identification of features, the minimum level of accuracy of classified map should be over 85% (Kumar et al., 2021). The accuracy assessment generally includes an error matrix, user accuracy, producer accuracy, overall accuracy, and kappa coefficient (Kumar et al., 2021). Here, the overall accuracy ranged between 0.925 and 0.998, kappa coefficient for all observation years were higher than 0.899, all meeting the minimum analysis requirements, deeming the classification accuracy is acceptable (Table 1, 2).

## **Postprocessing**

The post-processing of Landsat images includes images vectorization, area calculation and waterlines extraction. Images vectorization was transforming the classification map into vector map using "ee.Image.reduceToVectors()" function. Then "pixelArea" in GEE was used to calculated the area of deltaic islands. The waterline is the interface between water body and deltaic island, which is the dry-wet boundary (Geleynse et al., 2015). For waterline extraction, it was delineated manually from the outermost shoreline of each part of the delta in ArcGIS based on the deltaic island map, as we have divided the delta into three parts. For openings in the waterline (such as channel mouths), we first outlined the seaward boundaries of the deltaic islands and then connected them manually to get a complete waterline. Under the same tidal level, waterlines expanding seawards suggests the deltaic islands prograding seawards as well (Fig. 2B).

#### 2.3.2 Center of mass of deltaic islands

The center of mass model is widely applied to detect variations in population distribution, trends in regional economic growth, land use, and distribution and ecological environment (Na et al., 2019; Guo et al., 2020; Meng et al., 2021). This study uses the center of mass model to calculate the center of mass coordinates of the deltaic islands, and to analyze their change from 1990 to 2019. The equations of the center of mass are as follows:

$$\overline{X}_{l} = \frac{\sum_{i=1}^{n} X_{i} A_{i}}{\sum_{i=1}^{n} A_{i}}$$

$$\tag{5}$$

$$\overline{Y}_{l} = \frac{\sum_{i=1}^{n} Y_{i} A_{i}}{\sum_{i=1}^{n} A_{i}}$$

$$\tag{6}$$

Where:  $\overline{X}_i$ ,  $\overline{Y}_i$  refer to the center of mass coordinates;  $X_i$ ,  $Y_i$  are the longitude coordinate and latitude coordinate of the *i*th pixel; and  $A_i$  is the area of the *i*th pixel.

### 2.3.3 Rod Surface Elevation Table

In the CRMS network, the Rod Surface Elevation Table (RSET) method is used to estimate surface elevation change rates. One RSET benchmark is located at each CRMS site. From the RSET benchmark, surface elevation is measured at nine points in four directions to calculate elevation change at 6-month intervals. Specifically, the benchmark time is 2009/10/19 at the CRMS6304 in the WLD and 2009/2/19 at the CRMS0479 in the AD. In the CRMS, surface elevation change is defined as cumulative elevation change since station establishment. For each sampling event, mean cumulative elevation change is calculated for each of the four directions, and an elevation change rate is estimated using linear regression of elevation change against

297 time.

In addition, we constructed DEM using lidar data of the subaerial islands collected as USGS Atchafalaya 2 Lidar campaign (NOAA, 2011). Transects were selected about 200 m interval for each delta, extending 1 km from the shoreline in 2019 landwards (Auxiliary Fig. S1). According to the following formula, we have calculated the slope (S) of selected transects, and then calculated the vertical deposition rate (V, mm/yr) based on the slope and shoreline expansion rate (R, m/yr):

$$S = \frac{\Delta Z}{\Delta L} \tag{7}$$

$$V = S * R/1000 \tag{8}$$

Where:  $\Delta Z$  is height difference between the start and end of the transect (m);  $\Delta L$  is distance between the start and end of the transect (m). The results are shown in

Table 3.3 Results

## 3.1 Variations in water discharge and SSD

The water discharge and SSD delivered into the ARDC presented different variations between 1991-2019 at WLO and MC (Fig. 3). Specifically, the water discharge at WLO station exhibited a significantly upward trend (Fig. 3A). The monthly water discharge displayed a seasonal variation with a flood season between January and June and a dry season from July to December (Fig. 3B). The mean water discharge of the flood and dry seasons was 2971 m³/s and 1662 m³/s, respectively. In addition, the annual SSD ranged from  $0.85 \times 10^7$  t to  $3.50 \times 10^7$  t between 1991-2019, with an average value of  $2.06 \times 10^7$  t (Fig. 3C).

The records of the MC station indicated that the yearly water discharge changed little between 1991-2019, fluctuating around 995.77 × 10<sup>8</sup> m<sup>3</sup>/yr (Fig. 3D). The monthly water discharge displayed seasonal variations, with the mean water discharge during the flood and dry seasons equal to 3751 m<sup>3</sup>/s and 2164 m<sup>3</sup>/s, respectively (Fig. 3E). Furthermore, the mean yearly SSD ranged from 1.36×10<sup>7</sup> t to 6.26×10<sup>7</sup> t during 1991-2019, with a mean value of 3.19×10<sup>7</sup>t (Fig. 3F).

## 3.2 Migration of center of mass of deltaic islands

318

319

320

321

322

323

324

325

326

327

328

329

330

331

332

333

334

335

336

337

338

339

The shape of WLD has little changed from 1991 to 2019, only the seaward waterline presented progradation or recession (Fig. 4). The WP of the WLD was basically unchanged from 1991 to 2019. The waterline of the WP remained relatively smooth with little change at the water edge, except for some indentations in the distal part of the islands. In the same period, the waterline of the WP moved 780 m southwestward in the bay with an average rate of 26 m/yr, and the expansion rate ranged between -36 m/yr and 60 m/yr. The center of mass of WP migrated approximately 766 m southwest from 1991 to 2019(Fig. 4P). The center of mass initially moved southwest by 350 m between 1991 and 1995, but then shifted northeast by 140 m from 1995 to 1999. It moved southwest again by 320 m between 2003 and 2007, followed by a westward shift of 228 m from 2011 to 2015, and finally northeast by 132 m from 2015 to 2019. The configuration of the CP of the WLD is characterized by several distributary channels and related mouth bars forming deltaic islands. During 1991-2019, the islands expanded southward with an average rate of 45 m/yr. The expansion rate was approximately 125 m/yr from 1991-1995, and then slowed down and remained almost stable around 20 m/yr after 1999. The center of mass of CP migrated from northeast to the southwest approximately 1175 m from 1991 to 2019 (Fig. 4Q). Note that the center of mass changed significantly between 1991 and 1995, presenting a southwest movement of 894 m, which is followed by a slower migration, 143 m southwest, between 1995 and 1999. The center of mass moved northwest approximately 93 m and 85 m in the period of 1999-2003 and 2003-2007, respectively. The center of mass then shifted southwest about 194 m and 95 m in the period of 2007-2011 and 2011-2015. During 2015-2019, the center of mass shifted about 180 m northeast. The EP waterline moved seawards 580 m over the period between 1991-2019 with an average rate of 19 m/yr. The maximum expansion rate of waterline was 114 m/yr during 1991-1995 and then receded by 6 m/yr from 1999 to 2003 (Fig. 4K). The center of mass of the EP moved southeastward about 500 m during the period of 1991 to 2019 (Fig. 4R). A major migration occurred between 1991 and 1995, when the center of mass exhibited a southeast movement about 467 m, which then shifted about 154 m northwest from 1999 to 2007. During 2007-2019, the center of mass generally migrated southeast, though there was a 167 m northeastwards migration between 2015 and 2019. In AD, the waterline of WP expanded 750 m seaward from 1991 to 2019 (Fig. 5). In particular, the waterline suggested a retreat rate of 24 m/yr from 1999 to 2003 followed by a fast expansion of 30 m/yr during 2003-2007(Fig. 5K, L). The waterline migration slowed down and remained relatively stable with an expansion rate of only 3 m/yr after 2007 (Fig. 5 M-O). The center of mass of WP exhibited a series of dramatic shifts during 1995 to 2019, namely, a 2720 m southwest movement from 1995 to 1999,

340

341

342

343

344

345

346

347

348

349

350

351

352

353

354

355

356

357

358

359

360

a 3342 m northeast migration in the period of 1999-2003, a further 2225 m northeast migration during 2007-2011, a 2319 m southwest shift from 2011 to 2015 and then a 292 m northeast movement in the period of 2015-2019 (Fig. 5P). The waterline of CP moved 1300 m seawards from 1991 to 2019 with an expansion rate of 43 m/yr. The maximum expansion rate was 100 m/yr from 1991-1995, but a recession occurred in the period of 1999-2003 (Fig. 5I, K). The center of mass of CP moved approximately 287 m southwestward between 1991 and 1995, which was followed by a great 1600 m southwest migration between 1995 and 1999 and a significant 1428 m southeast migration from 2003 to 2007. After 2007, the center of mass shifted to the northwest (Fig. 5Q). The waterline of EP basically remained stable, moving 30 m seaward over the period 1991-2019 (Fig. 5I-K). The center of mass presented a southeastward migration by approximately 219 m over the period 1991-2019 (Fig.5R), with a notable northeast migration been detected between 1991 and 1995, when the center moved about 628 m. In the following periods of 1995-1999 and 2003-2007, the center of mass migrated southwest successively by 315 m and 306 m, and then shifted about 224 m southeast during 2007-2019.

#### 3.3 Areal change of deltaic islands

362

363

364

365

366

367

368

369

370

371

372

373

374

375

376

377

378

379

380

381

382

383

The total area of deltaic island in ARDC linearly increased from 45.07 km<sup>2</sup> in 1991 to 90.46 km<sup>2</sup> in 2019 at a significance level of 0.05, indicating an annual increasing trend of 1.29 km<sup>2</sup>/yr over the past 30 years (Fig. 6A). However, the change of island area in different regions of the ARDC displays some variability.

In the WLD, the deltaic islands increase from 21.90 km<sup>2</sup> in 1991 to 38.78 km<sup>2</sup> in

2019, with a linear rate of 0.60 km<sup>2</sup>/yr (p<0.05) (Fig. 6A). The area in the WP and EP increased with a constant rate of 0.12 km<sup>2</sup>/yr and 0.08 km<sup>2</sup>/yr in the period of 1991 to 2019 (Fig. 6B); while the area of CP gained about 12.45 km<sup>2</sup>, with a mean rate of 0.40 km<sup>2</sup>/yr (Fig. 6B). In the AD, the islands area increased from 23.17 km<sup>2</sup> in 1991 to 51.68 km<sup>2</sup> in 2019, with the increasing rate at 0.69 km<sup>2</sup>/yr (Fig. 6A). The deltaic island in the WP, CP and EP increased at rates of 0.17 km<sup>2</sup>/yr, 0.28 km<sup>2</sup>/yr and 0.24 km<sup>2</sup>/yr, respectively (Fig. 6C).

## 4 Discussion

Shape and growth of deltaic islands in low-relief alluvial deltas are primarily impacted by riverine flow, sediment supply, waves, human modifications and relative SLR (Fagherazzi et al., 2020; Nardin et al., 2016; Zhang et al., 2021; Carle et al., 2015). In this section, the potential processes controlling variations in deltaic islands area and shape in ARDC are discussed.

## 4.1 Effect of water discharge and sediment supply

The growth of a river-dominated delta was highly controlled by fluvial sediment and water flow (Lamb et al., 2012; Xu et al., 2021; Dai et al., 2018). The riverine sediments delivered into delta could deposit on the deltaic islands due to the slowing down of water flow caused by hindering effect of deltaic island and vegetations, which is favorable for delta formation (Long et al., 2021; Lou et al., 2022). Previous studies observed that coarse sediments were important for fueling delta growth because they overlay fine sediment to create a substrate elevated enough for colonization of marsh

species (van Heerden and Roberts, 1988). Fig. 7A-B describe the relationship between SSD and islands area over the study period 1991-2019. 7A-B. Fluvial SSD has positive relation with deltaic island area at a significant level of 0.05 at WLD, meaning that annual riverine suspended sediments have effectively promoted the growth of the WLD (Fig. 7A). However, there is no correlation between SSD and deltaic islands area at AD (Fig. 7B). The Atchafalaya River main channel has experienced obvious aggradation in 1977-2006 between the MC and AD by trapping a considerable amount of riverine delivered sediment (Tang et al., 2021), which significantly declined the sediments entering the delta. In such context, fluvial sediments can no longer support the formation of new land in AD. Other reasons therefore should be responsible for the AD deltaic island growth. This is further discussed in the following section. Large floods deliver a disproportionate amount of sediment to the coast, and play a critical role in the creation and maintenance of deltas and associated deltaic islands (Nittrouer et al., 2008, 2011; Carle et al., 2015). Nittrouer et al. (2008) found that high discharge events were important to delivering coarse sediment load in the lower Mississippi River, where bedform transport rate had a positive exponential correlation with discharge. In river-dominated deltas like the WLD, big floods lead to significant sediment deposition in the delta and on the islands (Carle et al., 2015; Bevington et al., 2017; Oliver et al., 2020). Here, peak discharge was positively correlated with each section of deltaic island in WLD (Fig. 8 A-C), indicating that the expansion of deltaic islands is mainly determined by flood events. During floods, high riverine discharge

mobilizes sediments that were deposited in river channels in low-flow conditions and

405

406

407

408

409

410

411

412

413

414

415

416

417

418

419

420

421

422

423

424

425

spread the material over a large area of the deltaic islands (Nittrouer et al., 2011, 2012; Rosen and Xu, 2013). However, Fig. 8 D-F demonstrates that the islands area of the three sub-sections of AD is unrelated to the peak discharge, indicating that fluvial flood has no significant effect on the growth of deltaic islands in this delta.

## 4.2 Impact of hurricanes and storms

427

428

429

430

431

432

433

434

435

436

437

438

439

440

441

442

443

444

445

446

447

448

Hurricanes and storms can erode large parts of deltaic islands (Barras, 2007; Howes et al., 2010) or supplying sediment to them (Nyman et al., 1995; Turner et al., 2006; Rosen and Xu, 2013). During 1991-2019, 12 hurricanes and 8 tropical storms landed near the ARDC (Table 3; Fig 9. E-G). In this study, we selected two images at similar tidal level before and after the landfall of hurricanes and tropical storms to quantify the storm effect on the islands. To quantify the effects of hurricanes and tropical storms, we calculated the area generated by fluvial sediments before and after the hurricanes using a positive correlation between SSD and deltaic island area. Then the area differences between the two images before and after hurricanes, was recognized as the impacts of hurricanes and tropical storms on deltaic islands. Guntenspergen et al. (1995) observed that Hurricane Andrew, which made landfall 20 km to the west of the ARDC, added on average 16 cm of sediments to the marshes surrounding Atchafalaya Bay. Barras (2003) found that hurricane Lili caused 7 km<sup>2</sup> of marsh loss ~ 21 km west of WLD (Rosen and Xu, 2013). Barras (2007) stated that much of the submerged and floating vegetation in the ARDC was removed by hurricane Rita, a category 3 hurricane with maximum wind speed of 185.2 km/h that made landfall 120

km to the west of WLD in 2005 and eroded more than 500000 m<sup>3</sup> of sediments in WLD

(Xing et al., 2017). Using two adjacent images before and after the landfall of tropical storm Isidore and Hurricane Lili in 2002, the deltaic island in the WLD and AD were calculated to have eroded 5.34 and 6.98 km<sup>2</sup>, respectively. In summary, hurricanes and tropical storms had a variable impact on both deltas.

Furtherly, we indicate that hurricanes and tropical storms triggered on average erosion on the WLD (Table 3). In particular, the deltaic island areal change has positive correlation with max wind speed which made landfall western of the deltas at a significance level of 0.1, and there is no correlation between islands areal change and the max storm wind speed in that year which landing eastern of the delta (Fig.9 A, B). In contrary, hurricanes and tropical storms with different category and direction caused both short-term deltaic island erosion and progradation in the AD. Specifically, we found a significant negative correlation between the max storm wind speed of a tropical cyclone that landed east to the ARDC and deltaic island area change (Fig. 9D), indicating that hurricane and tropical storms that landed east to the ARDC with higher wind speed would cause more erosion. However, the same relationship does not hold for hurricanes landing to the west of the delta (Fig. 9C), despite they trigger higher waves and storm surges on their right side.

Moreover, previous studies observed that high intensity storms and saltwater intrusion induced by associated storm surge can cause defoliation and vegetation shift and removement (Steyer et al., 2007; Barras, 2007). However, some vegetation with low-salt tolerance such as *Typha*, which can be found in fresh, moderately brackish, and brackish but not highly saline waters, can be damaged by saltwater intrusion (Bansal et

al., 2019). Others, like *Phragmites australis*, are more salt-tolerant and can survive in saline environments up to 22.5 parts per thousand (Lissner and Schierup, 1997). Marshes with high salt-tolerant vegetation can provide short-term protection against saline water hazards in deltaic regions (Visser et al., 2012). Moreover, studies suggested that the spectral reflectance of defoliation and dead vegetation in the near infrared (700-1300 nm) is obviously lower than green vegetation (Li and Guo, 2010). Their NDVI value are much lower than green vegetation. Therefore, the defoliation and dead vegetation affected by hurricanes can be neglected due to distinct characteristics of deltaic vegetation. As for the small amount of freshwater vegetation that can be destroyed due to saltwater intrusion caused by the storm surges, they may grow again in the following 1-2 months, thus has slight influence on the final results.

Although the historical images we obtained include the TM images before and after the hurricane landfall, these images were either cloudy or at high tidal level, thus making it difficult to satisfy our analysis of the salt marsh loss after the hurricane, which will affect the results to some extent. Thus, far-reaching studies on the loss of freshwater vegetation posed by saltwater intrusion caused by storm surges need to be carried out in the future. Considering the rapid recovery of salt marsh vegetation in summer, the use of unmanned aircraft or new high-resolution data may more accurately capture changes in salt marsh and loss of deltaic island at short intervals before and after the hurricane.

## 4.3 Sea level rise

Increasing sea levels can severely threaten deltaic islands if their elevations cannot accrete at the same rate of SLR

(Kirwan et al., 2013; Jankowski et al., 2017; Yang et al., 2021). Global mean SLR has increased by about 8 cm since 1993 (at a rate of 3.0±0.4 mm/yr), because of global warming (Sweet et al., 2017). SLR might exceed 2 m in many regions such as the contiguous United States by 2100 (Kopp et al., 2017; Lou et al., 2022). At the Grand Isle tidal station, mean sea level has risen at a rate of 8.17 mm/yr since 1991 (Fig. 10 A), while the deltas expanded seaward (Fig. 4, 5). Furtherly, a geodetic study has argued for present-day subsidence rate of 5-10 mm/yr in much of the states of Louisiana and Mississippi (Torbjörn et al., 2006). During the measurement period, surface elevation which implemented with RSET method has increased by 10.60 mm/yr and 2.80 mm/yr at the CRMS0479 and CRMS6304 (Fig. 10 B, C). Assuming constant slope, the vertical deposition rates of WP, CP, and EP in WLD are 10.90 mm/yr, 15.66 mm/yr, and 10.93 mm/yr (Table 4). At shoreline seaward spreading rate of 25.00 m/yr, 43.00 m/yr, and 1.00 m/yr, the WP, CP, and EP in AD vertically accreted 23.28 mm, 35.15 mm, and 0.65 mm per year, respectively. Result suggested that the rate of vertical accretion exceeds SLR, indicating that the delta is not currently facing the threat of inundation, except for the EP of AD (Table 4).

Table 4 Slope and vertical deposition rate of each part in WLD and AD

					Vertical		
Delta	Regine	Transect	Slope	Expansion rate (m/yr)	deposition rate		
					(mm/yr)		
	WP	1-12	0.00041920	26.00	10.90		
WLD	MP	15-36	0.00034802	45.00	15.66		
	СР	38-51	0.00057541	19.00	10.93		
	WP	1-25	0.00093100	25.00	23.28		
AD	MP	28-47	0.00081748	43.00	35.15		
	СР	48-66	0.00065490	1.00	0.65		

#### 4.4 Anthropogenic activities

Human activities have the potential to alter and exert a dominant influence on the evolution of deltaic islands (Allen et al., 2012; Carle et al., 2015; Elliton et al., 2020). In the WLD, neither human settlements nor direct manipulation (dredging or levees construction) has occurred since the formation of the delta. Only a few structures, houseboats and moorings exist in the northwestern WLD (Auxiliary Fig. S2). Under the minor interference the WLD remained natural in character, with a symmetric, lobate shape. Meanwhile, the center of mass of the WLD has migrated regularly (Fig. 4P-R). In summary, under sufficient sediment supply and minor anthropogenic impact, deltaic islands could present self-organized expansion and vertical accretion trend as in the

WLD (Fig.4, Fig. 10 B).

Unlike the WLD, the growth of the AD was highly affected by dredge spoil activities (Zhang et al., 2021, Fig. 11A). To meet navigation requirements, the USACE has dredged the sediment deposited in the ARMC and used it to create new wetlands since 1975 (Boustany, 2010; Allen et al., 2012). Zhang et al. (2021) found that dredge spoil activities has created about 19.48 km² of deltaic lands in AD from 1985 to 2017. Using visual interpretation, we found that the newly formed deltaic island area by dredge spoils was 0.69 km² in 2018 and 0.37 km² 2019 (Fig. 11B). The significant westward expansion of deltaic island in the AD during 1991-1999 is probably due to the carry out of extensive dredge spoil on the western delta, which is slowed down in the subsequent years and thus generated a slower expansion of deltaic island (Fig. 5). Therefore, spoil disposal has altered the natural evolution of the AD, and also disturbed the natural migration of the center of mass.

# Conclusion

As one of the few deltaic areas expanding seaward, the deltaic islands in the ARDC are of great significance to the study of coastal land restoration. Here, we analyzed the temporal and spatial variations characteristic of the deltaic island in WLD and AD between 1991 to 2019 and identified possible drivers for deltaic island evolution. The main conclusions are as follows:

1) The area of deltaic island in the ARDC exhibited a substantial increase with a rate of 1.29 km²/yr from 1991 to 2019. The deltaic islands area of WLD and AD expanded

with an increasing rate of 0.60 km<sup>2</sup>/yr and 0.69 km<sup>2</sup>/yr, respectively. The increasing

rate of AD is slightly higher than that of WLD, which can be explained by the dredging and disposal activities in AD that provided extra material sources for the growth of deltaic islands. The WP, CP, and EP of WLD expanded seawards at the rate of 26 m/yr, 45 m/yr, 19 m/yr, The WP, CP, and EP of AD prograded 25 m/yr, 43 m/yr and 1 m/yr. The higher progradation rates of the central parts indicate that the two deltas are elongating in Atchafalaya Bay, with a shape typical of fluvial dominated deltas; 2) Fluvial SSD and peak discharge events triggered the expansion and dominated the spatial evolution pattern of deltaic island in WLD. Anthropogenic activities have altered the natural growth pattern of deltaic island in the AD, and dredge and sediment disposal can be responsible for the expansion of deltaic island; 3) The deltaic islands of ARDC were not facing threat of sea level inundation, as the rate of vertical accretion was higher than SLR, except for the EP of AD may be at risk of drowning. Hurricane and tropical storm events caused mainly erosive impacts on the WLD, but transient erosion or siltation on the AD. High-intensity hurricanes

#### Acknowledgement

538

539

540

541

542

543

544

545

546

547

548

549

550

551

552

553

554

555

556

557

558

559

This research was supported by the Joint Key Funds of National Natural Science Foundation of China (U2040202), the Key Projects of Intergovernmental Science and Technology Innovation Cooperation of the Ministry of Science and Technology in China (2018YFE0109900), and the USA National Science Foundation awards 1637630 (PIE LTER) and 1832221 (VCR LTER).

that made landfall east of the delta cause more erosion on the AD.

#### References

- Allen, Y. C., Couvillion, B. R., Barras, John A., 2012. Using multitemporal remote
- sensing imagery and inundation measures to improve land change estimates in
- 563 coastal wetlands. Estuar. Coast, 35 (1), 190-200.
- Anthony, E. J., Brunier, G., Besset, M., Goichot, M., Dussouillez 1, P., Nguyen, V. L.,
- 565 2015. Linking rapid erosion of the Mekong River delta to human activities.
- Scientific Reports, 5:14745.
- Bansal, S., Lishawa, S. C., Newman, S., et al, 2019. Typha (Cattail) Invasion in North
- American Wetlands: Biology, Regional Problems, Impacts, Ecosystem Services,
- and Management. Wetlands, 1-40.
- Barras, J.A., 2003. Changes to Cote Blanche Hydrologic Restoration (TV-04) Area
- After Hurricane Lili. U.S. Geological Survey, National Wetlands Research Center,
- Map ID USGS NWRC 2.
- Barras, J.A., 2007. Land area changes in coastal Louisiana after Hurricanes Katrina and
- Rita. In: Farris, G.S., Smith, G.J., Crane, M.P., Demas, C.R., Robbins, L.L., Lavoie,
- D.L. (Eds.), Science and the Storms-The USFS Response to the Hurricanes of
- 576 2005. U.S. Geological Survey Circular 1306, pp. 98-113.
- Belgiu, M. and Dr agu t, L. 2016. Random forest in remote sensing: A review of
- applications and future directions, ISPRS J. Photogramm., 114, 24-31.
- Bevington, A.E., Twilley, R.R., Sasser, C.E., Holm, G.O., 2017. Contribution of river
- floods, hurricanes, and cold fronts to elevation change in a prograding deltaic

581 floodplain in the northern Gulf of Mexico, USA. Estuar. Coast. Shelf Sci. 191, 582 188-200. Bwangoy, J.B.; Hansen, M.C.; Roy, D.P.; Grandi, G.D.; Justice, C.O., 2010. Wetland 583 mapping in the Congo Basin using optical and radar remotely sensed data and 584 585 derived topographical indices. Remote Sens. Environ. 114, 73-86. Carle, M.V., CE Sasser, Roberts, H. H., 2015. Accretion and vegetation community 586 change in the wax lake delta following the historic 2011 Mississippi River flood. 587 588 Journal of Coastal Research, 31(3), 569-587. 589 Chen, B., Xiao, X., Li, X., et al., 2017. A mangrove forest map of china in 2015: analysis 590 of time series landsat 7/8 and sentinel-1a imagery in google earth engine cloud 591 computing platform. ISPRS J. Photogramm. Remote Sens. 131, 104-120. 592 Costanza, R., O. Pérez-Magueo, M. L. Martinez et al., 2008. The value of coastal 593 wetlands for hurricane protection, AMBIO: A J. Human Environ., 37(4), 241-248. 594 Dai Z., 2021. Changjiang riverine and estuarine hydro-morphodynamic processes, In 595 the Context of Anthropocene Era. Springer Press. 596 Dai, Z., Liu, J., Fu, G., Xie, H., 2013. A thirteen-year record of bathymetric changes in 597 the North passage, Changjiang (Yangtze) estuary. Geomorphology 187, 101-107. Dai, Z., Mei, X., Darby, S.E., Lou, Y., Li, W., 2018. Fluvial sediment transfer in the 598 599 Changjiang (Yangtze) river-estuary depositional system. J. Hydrol. 566, 719-734. 600 DeLaune, R.D., Sasser, C. E., Evers-Hebert, E., White, J.R., Roberts, H.H., 2016. Influence of the Wax Lake Delta sediment diversion on aboveground plant 601

- productivity and carbon storage in deltaic island and mainland coastal marshes.
- 603 ESTUAR COAST SHELF S, 177(-):83-89.
- 604 Elliton, C.; Xu, K.; Rivera-Monroy, V.H, 2020. The Impact of Biophysical Processes
- on Sediment Transport in the Wax Lake Delta (Louisiana, USA). Water, 12,2072.
- 606 Ericson, J.P., Vörösmarty, C.J., Dingman, L., Ward, L. G., Meybeck, M., 2006.
- Effective sea-level rise and deltas: Causes of change and human dimension
- implications. Global and Planetary Change, 50(1):63-82.
- 609 Fagherazzi, S., Edmonds, D.A., Nardin, W., Leonardi, N., Canestrelli, A., Falcini, F., et
- al., 2015. Dynamics of river mouth deposits: reviews of geophysics.
- Fagherazzi, S., Mariotti, G., Leonardi, N., Canestrelli, A., Nardin, W., & Kearney, W.
- S., 2020. Salt marsh dynamics in a period of accelerated sea level rise. Journal of
- Geophysical Research: Earth Surface, 125, e2019JF005200.
- Farda, N. M., 2017. Multi-temporal Land Use Mapping of Coastal Wetlands Area using
- Machine Learning in Google Earth Engine. IOP Conf. Ser.: Earth Environ. Sci. 98
- 616 012042.
- 617 FitzGerald, S.M., 1998. Sand body geometry of the Wax Lake Outlet delta, Atchafalaya
- Bay, Louisiana. Louisiana State University, Baton Rouge, Louisiana.
- 619 Fu Y., Cao W., Pan D., Ren Y., 2022. Changes of groundwater arsenic risk in different
- seasons in Hetao Basin based on machine learning model. Science of the Total
- Environment.
- 622 Geleynse, N., Hiatt, M., Sangireddy, H., Passalacqua, P., 2015. Identifying

- 623 environmental controls on the shoreline of a natural river delta. Journal of
- Geophysical Research: Earth Surface, 120(5), 877-893.
- 625 Gorelick, N., Hancher, M., Dixon, M., Ilyushchenko, S., Thau, D., Moore, R., 2017.
- Google Earth Engine: planetary-scale geospatial analysis for everyone. Remote
- 627 Sens. Environ. 202, 18-27.
- 628 Guntenspergen, G.R., Cahoon, D.R., Grace, J., Steyer, G.D., Fournet, S., Townson,
- M.A., Foote, A.L., 1995. Disturbance and recovery of the Louisiana coastal marsh
- landscape from the impacts of Hurricane Andrew. Journal of Coastal Research,
- 631 Special Issue No. 21, pp. 324-339.
- Guo H., Huang, J. J., Zhu, X., Wang B., Tian S., Xu W., Mai. Y., 2021. A generalized
- machine learning approach for dissolved oxygen estimation at multiple
- spatiotemporal scales using remote sensing. Environmental Pollution.
- 635 Guo, B., Zang, W., Han, B., Yang, F., Luo, W., He, T., Fan, Y., Yang, X., Chen, S., 2020.
- Dynamic monitoring of desertification in Naiman Banner based on feature space
- models with typical surface parameters derived from LANDSAT images. Land
- 638 Degrad. Dev. n/a 31 (12), 1573-1592.
- Horowitz, A.J., 2010. A quarter century of declining suspended sediment fluxes in the
- Mississippi River and the effect of the 1993 flood. Hydrological Processes 24, 13-
- 641 34.
- Howes, N.C., FitzGerald, D.M., Hughes, Z.J., Georgiou, I.Y., Kulp, M.A., Miner, M.D.,
- Smith, J.M., Barras, J.A., 2010. Hurricane-induced failure of low salinity wetlands.
- PNAS 107 (32), 14014-14019.

- Huete, A., Didan, K., Miura, T., Rodriguez, E.P., Gao, X., Ferreira, L.G., 2002.
- Overview of the radiometric and biophysical performance of the MODIS
- vegetation indices. Remote Sensing of Environment, 83, 195-213.
- Jankowski, K., To rnqvist, T., Fernandes, A., 2017. Vulnerability of Louisiana's coastal
- wetlands to present-day rates of relative sea-level rise. Nat. Commun. 8, 14792.
- 650 Keim, B.D., Muller, R.A., Stone, G.W., 2007. Spatiotemporal patterns and return
- periods of tropical storm and hurricane strikes from Texas to Maine. J. Clim. 20,
- 652 3498-3509.
- Kirwan, M., Megonigal, J., 2013. Tidal wetland stability in the face of human impacts
- and sea-level rise. *Nature* 504, 53-60.
- 655 Kopp, R.E., DeConto, R.M., Bader, D.A., Hay, C.C., Horton, R.M., Kulp, S.,
- Oppenheimer, M., Pollard, D., Strauss, B.H., 2017. Evolving understanding of
- antarctic ice-sheet physics and ambiguity in probabilistic sea-level projections.
- 658 Earth's Future 5 (12), 1217-1233.
- Kumar, P., Dobriyal, M., Kale, A., Pandey, A.K., 2021. Temporal dynamics change of
- land use/land cover in Jhansi district of Uttar Pradesh over past 20 years using
- LANDSAT TM, ETM+ and OLI sensors. Remote Sensing Applications: Society
- and Environment, 23.
- Lamb, M. P., Nittrouer, J. A., Mohrig, D., Shaw, J., 2012. Backwater and river plume
- controls on scour upstream of river mouths: Implications for fluvio-deltaic
- morphodynamics, J. Geophys. Res., 117, F01002.

- 666 Lawrence, R.L., Wrlght, A., 2001. Rule-based classification systems using
- classification and regression tree (cart) analysis. Photogramm Eng Remote
- 668 Sensing, 2001,67(10), 1137-1142.
- 669 Li Z., Guo X. 2010. A suitable vegetation index for quantifying temporal variation of
- leaf area index (LAI) in semiarid mixed grassland. Canadian Journal of Remote
- 671 Sensing, 36(6):709-721.
- Lissner, J., Schierup, H.H., 1997. Effects of salinity on the growth of Phragmites
- 673 australis. Aquatic Botany, 55(4):247-260.
- Long, C. Q., Dai, Z. J., Zhou, X. Y., Mei, X.F., Van, C.M., 2021. Mapping mangrove
- forests in the Red River Delta, Vietnam. Forest Ecology and Management, 483.
- 676 Long, C. Q., Dai, Z. J., Wang, R. M., Lou, Y.Y., Zhou, X.Y., Li, S.S., Nie.Y., 2022.
- Dynamic changes in mangroves of the largest delta in northern Beibu Gulf, China:
- Reasons and causes. Forest Ecology and Management, 504.
- 679 Lou Y Y, Dai Z J\*, Long C Q, et al. Image-based machine learning for monitoring the
- dynamics of the largest salt marsh in the Yangtze River Delta, Journal of
- 681 Hydrology, 2022, 608.
- Magidi J., Nhamo L., Mpandeli S., Mabhaudhi T., 2021. Application of the Random
- Forest Classifier to Map Irrigated Areas Using Google Earth Engine. Remote
- 684 Sensing, 13(5):876.
- Meng, X., Gao, X., Li, S., Lei, J., 2020. Spatial and temporal characteristics of
- vegetation NDVI changes and the driving forces in Mongolia during 1982-2015.

- 687 Remote Sens. 12, 603.
- 688 Mossa, J., Roberts, H.H., 1990. Synergism of riverine and winter storm related
- sediment transport processes in Lousiana coastal wetlands. Trans. Coast Assoc.
- 690 Geol. Soc. 40, 635-642.
- 691 Na, R., Du, H., Na, L.i., Shan, Y., He, H.S., Wu, Z., Zong, S., Yang, Y., Huang, L., 2019.
- Spatiotemporal changes in the Aeolian desertification of Hulunbuir Grassland and
- its driving factors in China during 1980-2015. CATENA 182, 104123.
- Nardin W., Edmonds D. A., Fagherazzi S., 2016. Influence of vegetation on spatial
- patterns of sediment deposition in deltaic islands during flood. Advances in Water
- 696 Resources, 93:236-248.
- Nienhuis, J.H., Ashton, A.D., Edmonds, D.A., Hoitink, A.J.F., Törnqvist, T.E., 2020.
- Global-scale human impact on delta morphology has led to net land area gain.
- 699 Nature 577, 514-518.
- Nittrouer, J.A., Allison, M.A., Campanella, R., 2008. Bedform transport rates for the
- 701 lowermost Mississippi River. Journal of Geophysical Research 113, 1-16.
- Nittrouer, J.A., Mohrig, D., Allison, M.A., 2011. Punctuated sand transport in the
- lowermost Mississippi River. Journal of Geophysical Research, 116(F4), F04025.
- Nittrouer, J.A., Shaw, J., Lamb, M.P., Mohrig, D., 2012. Spatial and temporal trends for
- water-flow velocity and bed-material sediment transport in the lower Mississippi
- River. Geological Society of America Bulletin, 124(3-4), 400-414.
- Nyman, J.A., Crozier, C.R., DeLaune, R.D., 1995. Roles and patterns of hurricane

- sedimentation in an estuarine marsh landscape. Estuarine, Coastal and Shelf
- 709 Science 40 (6), 665-679.
- 710 Olliver, E.A., Edmonds, D.A., Shaw, J.B., 2020. Influence of floods, tides, and
- vegetation on sediment retention in Wax Lake Delta, Louisiana, USA. J. Geophys.
- 712 Res. Earth Surf. 125 (1), e2019JF005316.
- 713 Olson, K.R. and Suski, C.D., 2021. Mississippi River Delta: Land Subsidence and
- Coastal Erosion. Open Journal of Soil Science, 11, 139-163.
- Pertiwi, A.P.; Roth, A.; Schaffhauser, T.; Bhola, P.K.; Reuß, F.; Stettner, S.; Kuenzer,
- 716 C.; Disse, M, 2021. Monitoring the Spring Flood in Lena Delta with
- 717 Hydrodynamic Modeling Based on SAR Satellite Products. Remote Sens. 13,
- 718 4695.
- Reeve, D.E., Karunarathna, H., 2009. On the prediction of long-term morphodynamic
- response of estuarine systems to sea level rise and human interference. Cont. Shelf
- 721 Res. 29 (7), 938-950.
- Roberts, H.H., Adams, R.D., Cunningham, R.H.W., 1980. Evolution of sand-dominant
- subaerial phase, Atchafalaya Delta, Louisiana. American Association of Petroleum
- 724 Geologists Bulletin 64 (2), 264-279.
- Roberts, H.H., Coleman, J.M., Bentley, S.J. and Walker, N., 2003. An embryonic major
- delta lobe: A new generation of delta studies in the Atchafalaya-Wax Lake Delta
- 727 system.
- Rosen T., Xu Y. J., 2013. Recent decadal growth of the Atchafalaya River Delta

- complex: Effects of variable riverine sediment input and vegetation succession.
- 730 Geomorphology, 194(4):108-120.
- Rouse, J.W, Haas, R.H., Scheel, J.A., Deering, D.W., 1974. Monitoring Vegetation
- 732 Systems in the Great Plains with ERTS. Proceedings, 3rd Earth Resource
- 733 Technology Satellite (ERTS) Symposium 1, 48-62.
- 734 Sendrowski A., Passalacqua P., Castanedamoya E., et al, 2016. Linking hydrologic
- connectivity and nutrient dynamics in a deltaic island of prograding Wax Lake
- 736 Delta, coastal Louisiana.
- 737 Shaw, J.B. and Mohrig, D., 2014. The importance of erosion in distributary channel
- network growth, Wax Lake Delta, Louisiana, USA. Geology, 42(1), pp.31-34.
- 739 Shlemon, R.J., 1975. Subaqueous delta formation-Atchafalaya Bay, Louisiana. In:
- Broussard, M.L. (Ed.), Deltas: Models of Exploration. Houston Geological
- 741 Society, Houston, TX, pp. 209-221.
- Steyer G.D., Perez B.C., Piazza S.C., Suir G., 2007. Potential consequences of saltwater
- intrusion associated with Hurricanes Katrina and Rita: chapter 6C in Science and
- the storms-the USGS response to the hurricanes of 2005. Circular 1306-136C.
- Sweet W. V., Kopp R. E., Weaver C. P., et al, 2017. Global and regional sea level rise
- scenarios for the United States.
- 747 Syvitski, J.P.M., Kettner, A.J., Overeem, I., Hutton, E.W.H., Hannon, M.T.,
- Brakenridge, G.R., Day, J., Vorosmarty, C., Saito, Y., Giosan, L., Nicholls, R.J.,
- 749 2009. Sinking deltas due to human activities. Nature Geoscience.

- 750 Tang M., Xu Y. J., Xu W., Wang, B., Cheng, H.Q., 2021. Three-decadal erosion and
- deposition of channel bed in the Lower Atchafalaya River, the largest distributary
- of the Mississippi River. Geomorphology, 107638.
- 753 Törnqvist, T.E., Bick, S. J., Borg, K., Jong, A., 2006. How stable is the Mississippi
- 754 Delta? Geology, 34 (8): 697-700.
- 755 Turner, R.E., Baustian, J.J., Swenson, E.M., Spicer, J.S., 2006. Wetland sedimentation
- from hurricanes Katrina and Rita. Science 314 (5798), 449-452.
- van Heerden, I.L., Roberts, H.H., 1988. Facies development of Atchafalaya Delta,
- 758 Louisiana: a modern bayhead delta. American Association of Petroleum
- 759 Geologists Bulletin 72 (4), 439-453.
- Visser, J. M., Sasser, C. E., Linscombe, R. G., Chabreck, R.H., 2012. Marsh Vegetation
- Types of the Chenier Plain, Louisiana, USA. Estuaries and Coasts, 23(3):318-327.
- Walker, N.D., 2001. Tropical storm and hurricane wind effects on water level, salinity,
- and sediment transport in the river-influenced Atchafalaya-Vermilion Bay system,
- 764 Louisiana, USA. Estuaries 24 (4), 498-508.
- Wang, B, Xu, Y. J., Xu, W., Cheng, H.Q., Chen, Z.Y., Zhang, W.G., 2020. Channel bed
- dynamics below a large engineering-controlled river confluence The uppermost
- 767 Atchafalaya River, USA. Water, 12, 2139.
- Xiao, X.M., Hollinger, D., Aber, J., Goltz, M., Davidson, E.A., Zhang, Q.Y., Moore, B.,
- 769 2004. Satellite-Based Modeling of Gross Primary Production in an Evergreen
- Needleleaf Forest. Remote Sensing of Environment, 89, 519-534.

- Xing, F., Syvitski, J. P.M., Kettner, A.J., Meselhe, E. A., Atkinson, J. H., Khadka, A. K.,
- 772 2017. Morphological responses of the Wax Lake Delta, Louisiana, to Hurricanes
- Rita. Elem Sci Anth, 5:80.
- Xu Z.H., Wu S.H., Liu M.C. et al., 2021. Effects of water discharge on river-dominated
- delta growth. Petroleum Science, 18, 1630-1649.
- Xu, H., 2006. Modification of normalized difference water index (NDWI) to enhance
- open water features in remotely sensed imagery. International journal of remote
- 778 sensing, 27(14), 3025-3033.
- Xu, Y.J., 2010. Long-term Sediment Transport and Delivery of the Largest Distributary
- of the Mississippi River, the Atchafalava, USA. In: Banasik, K., Horowitz, A.,
- Owens, P.N., Stone, M., Walling, D.E. (Eds.), Sediment Dynamics for a Changing
- Future, 337. IAHS Publication, Wallingford, UK, pp. 282-290.
- Xu, Y.J., Bryantmason, A., 2011. Determining the Nitrate Contribution of the Red River
- to the Atchafalaya River in the Northern Gulf of Mexico under Changing Climate.
- In: Peters, J. (Ed.), Water Quality: Current Trends and Expected Climate Change
- 786 Impacts, 348. IAHS Publication, Wallingford, UK, pp. 95-100.
- Yang, H. F., Yang, S. L., Li, B. C., et al., 2021. Different fates of the Yangtze and
- 788 Mississippi deltaic wetlands under similar riverine sediment decline and sea-level
- 789 rise. Geomorphology, 381(18):107646.
- 790 Zhang, L., Hu, Q., Tang, Z., 2022. Assessing the contemporary status of Nebraska's
- eastern saline wetlands by using a machine learning algorithm on the Google Earth
- Engine cloud computing platform. Environ Monit Assess 194, 193.

Zhang, X., Xu, K., Yang, Z., Tan, X., Wu, C., 2021. Decreasing land growth and unique 793 seasonal area fluctuations of two newborn Mississippi subdeltas. Geomorphology, 794 378(1):107617. 795 796 Zhou, X. Y., Dai, Z. J., Mei, X. F., 2020. The multi-decadal morphodynamic changes 797 of the mouth bar in a mixed fluvial-tidal estuarine channel. Marine Geology, 429, 798 106311. Zou, Z.H., Dong, J.W., Menarguez, M.A., Xiao, X.M., Qin, Y.W., Doughty, R.B., 799 800 Hooker, K.V., Hambright, K.D., 2017. Continued decrease of open surface water body area in Oklahoma during 1984-2015. Sci. Total Environ. 595, 451-460. 801 Figure captions 802 803 Figure 1. Study area. A. Lower Mississippi River; B. lower Atchafalaya River. C. The WLD is divided into three parts: western part (WP), central part (CP) and 804 805 eastern part (EP); D. The AD is also divided into three parts: western part (WP), central part (CP) and eastern part (EP). ARDC center is defined by the 806 point of equal distance of WLD and AD 807 808 Figure 2. Image processing workflow and schematic maps of deltaic island and water bodies. A. The workflow of the images processing; B. The determination of 809 810 waterline. C. Landsat image of WLD; D. Map of deltaic islands and water in 811 WLD distinguished by the RF algorithm; E. Landsat image of AD; F. Map of 812 deltaic island and water in AD distinguished by the RF algorithm 813 Figure 3. Changes in water discharge and SSD. A. Annual water discharge at WLO; B.

814	Monthly water discharge at WLO; C. Yearly SSD at WLO; D. Annual water
815	discharge at MC; E. Monthly water discharge at MC; F. Yearly SSD at MC
816	Figure 4. Morphological change of deltaic islands in WLD between 1991-2019. P-R.
817	Migration of center of mass of WP, CP and EP
818	Figure 5. Morphological change of deltaic islands in AD between 1991-2019. P-R.
819	Migration of center of mass of WP, CP and EP
820	Figure 6. Temporal changes in deltaic island area
821	Figure 7. The relation of SSD and deltaic island area
822	Figure 8. The relation between peak discharge and deltaic island area of each part
823	Figure 9. Relation between max storm wind speed of a tropical cyclone and area
824	change of deltaic islands. A-B. Relation between max storm wind speed of a
825	tropical cyclone landing west and east of the ARDC and area change of
826	deltaic islands in WLD; C-D. Relation between max storm wind speed of a
827	tropical cyclone landing west and east of the ARDC and area change of
828	deltaic islands in AD; E-G. Hurricane and tropical storm tracks in 1991-1999,
829	1999-2007 and 2007-2019
830	Figure 10. Sea level rise and deltaic island elevation change. A. Annual mean sea levels
831	at the Grand Isle tidal station between 1991 and 2019; B. Surface elevation
832	change measured at the CRMS0479 in the WLD; C. Surface elevation change
833	measured at the CRMS6304 in the AD. The elevation of highlighted cluster
834	in 2016 was significantly lower compared to the surrounding years,
835	suggesting that these may be anomalous data, and they were excluded to

836	prevent them from influencing the results of the correlation analysis
837	Figure 11. Deltaic lands formed by dredge spoils. A. Dredge spoil model. The red
838	polygons indicated the newly formed deltaic lands due to the dredge spoils.
839	B. Deltaic lands formed by dredge spoils in the AD from 1991 to 2019.
840	Dredging spoil land area from 1991 to 2017 was collected by Zhang et al.
841	(2021)
842	Auxiliary Fig. S1 The DEM map based on USGS Atchafalaya 2 Lidar. A. Transects in
843	WLD; B. Transects in AD. Transects were selected about 200 m interval.
844	extending 1 km from the shoreline in 2019 landwards
845	Auxiliary Fig. S2 Northwestern WLD in 2005/11. The image showed a few structures
846	houseboats and moorings in northwestern WLD
847	

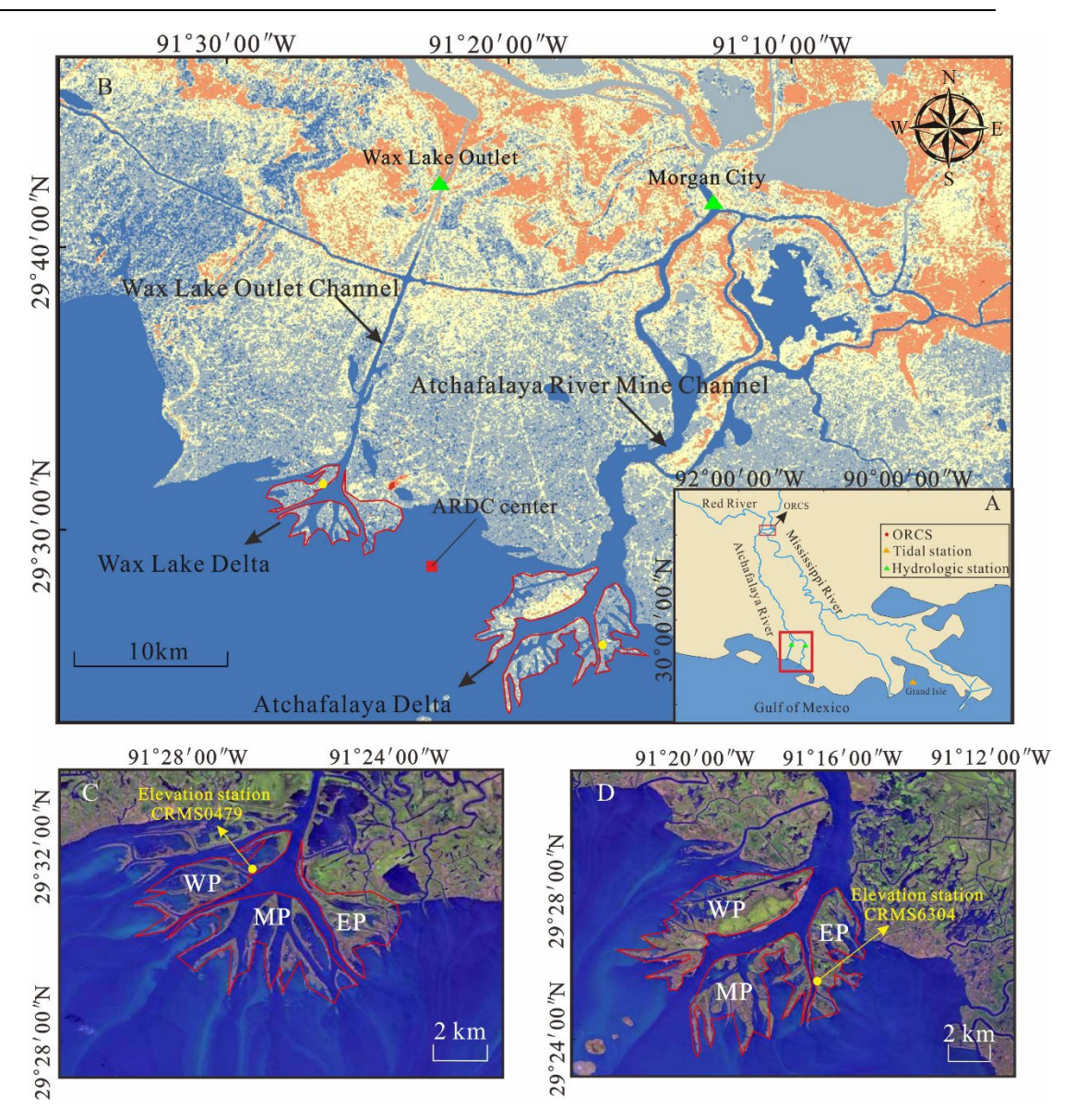


Figure 1. Study area. A. Lower Mississippi River; B. lower Atchafalaya River. C. The WLD is divided into three parts: western part (WP), central part (CP) and eastern part (EP); D. The AD is also divided into three parts: western part (WP), central part (CP) and eastern part (EP). ARDC center is defined by the point of equal distance of WLD and AD

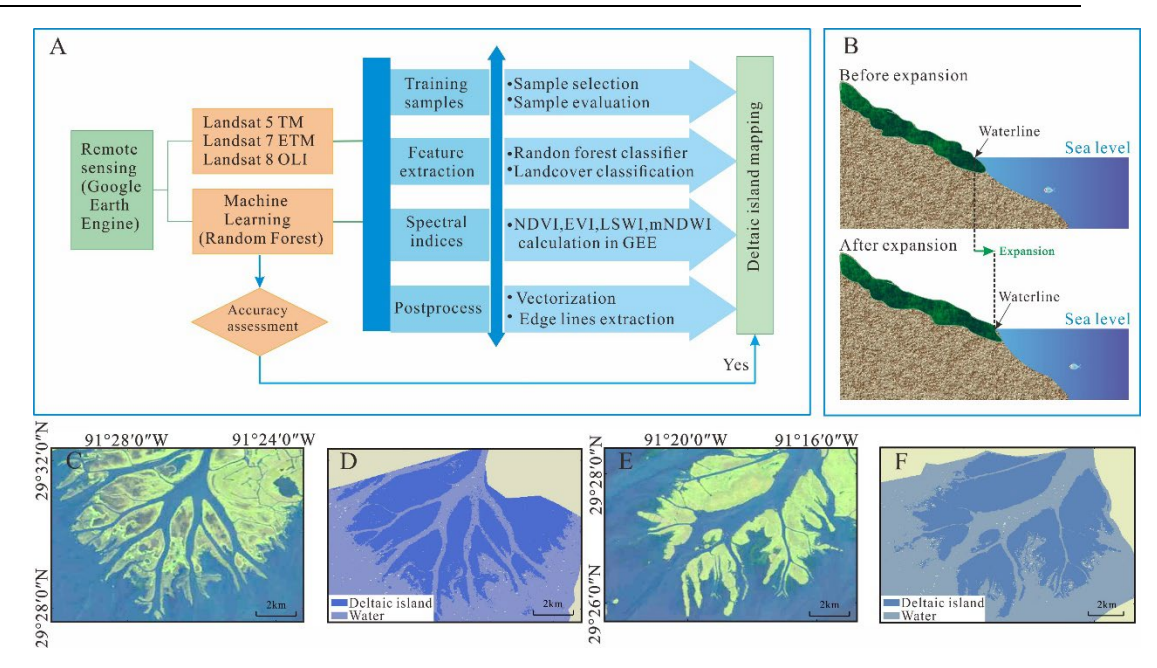


Figure 2. Image processing workflow and schematic maps of deltaic island and water bodies. A. The workflow of the images processing; B. The determination of waterline. C. Landsat image of WLD; D. Map of deltaic islands and water in WLD distinguished by the RF algorithm; E. Landsat image of AD; F. Map of deltaic island and water in AD distinguished by the RF algorithm

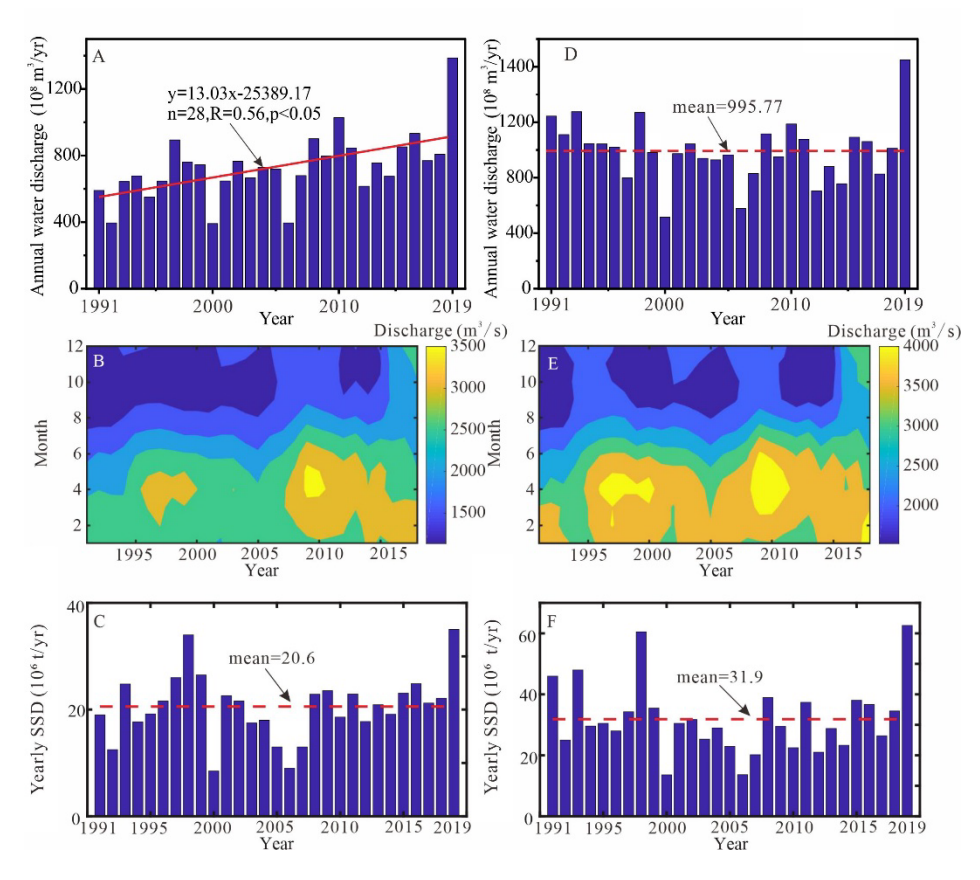


Figure 3. Changes in water discharge and SSD. A. Annual water discharge at WLO; B. Monthly water discharge at WLO; C. Yearly SSD at WLO; D. Annual water discharge at MC; E. Monthly water discharge at MC; F. Yearly SSD at MC

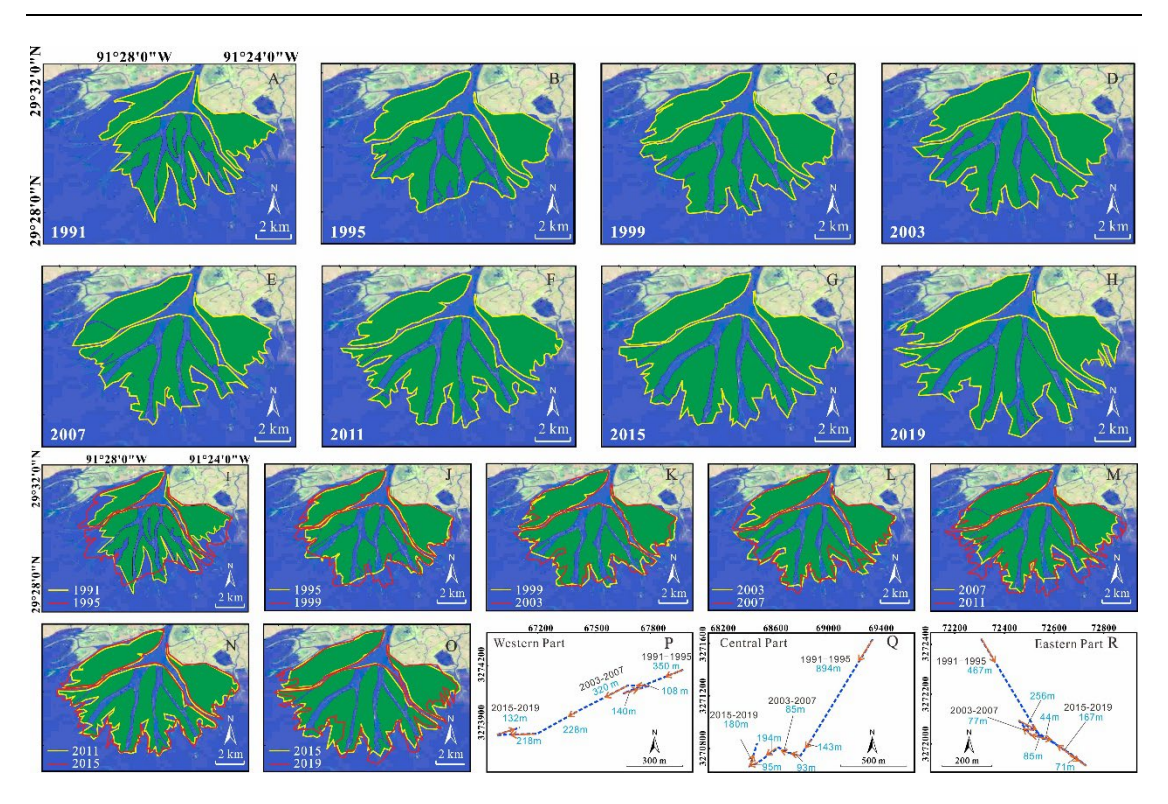


Figure 4. Morphological change of deltaic islands in WLD between 1991-2019. P-R. Migration of center of mass of WP, CP and EP

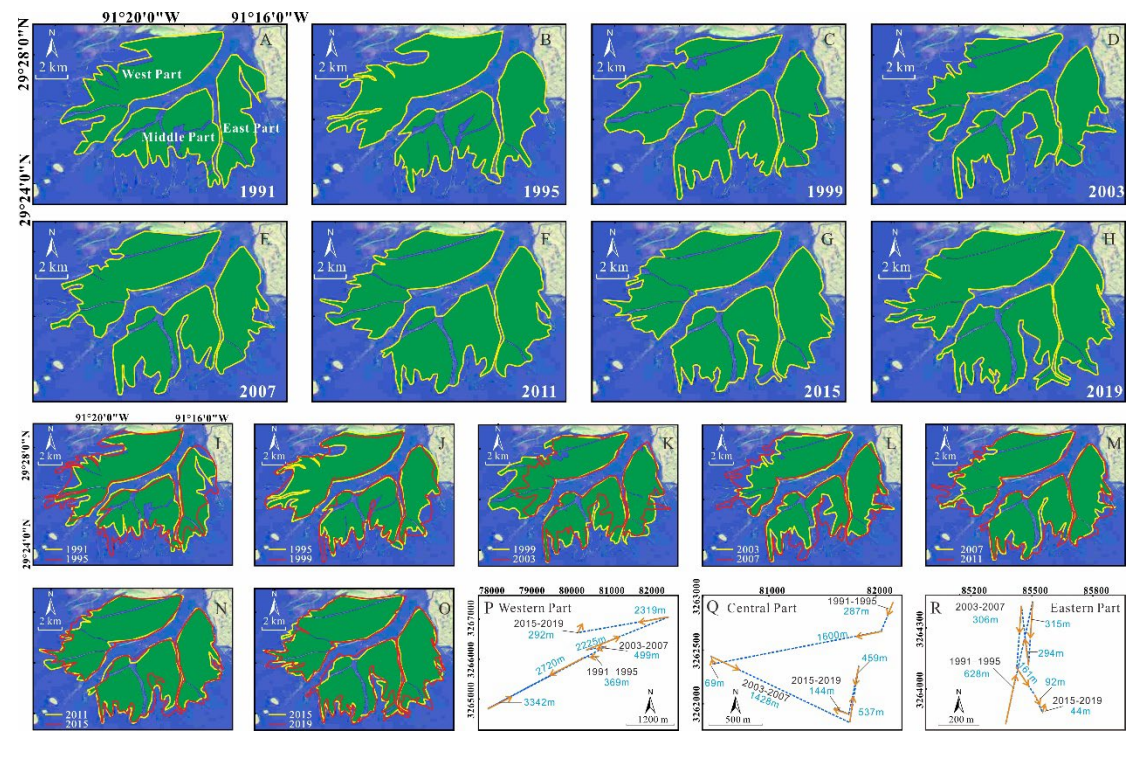


Figure 5. Morphological change of deltaic islands in AD between 1991-2019. P-R. Migration of center of mass of WP, CP and EP

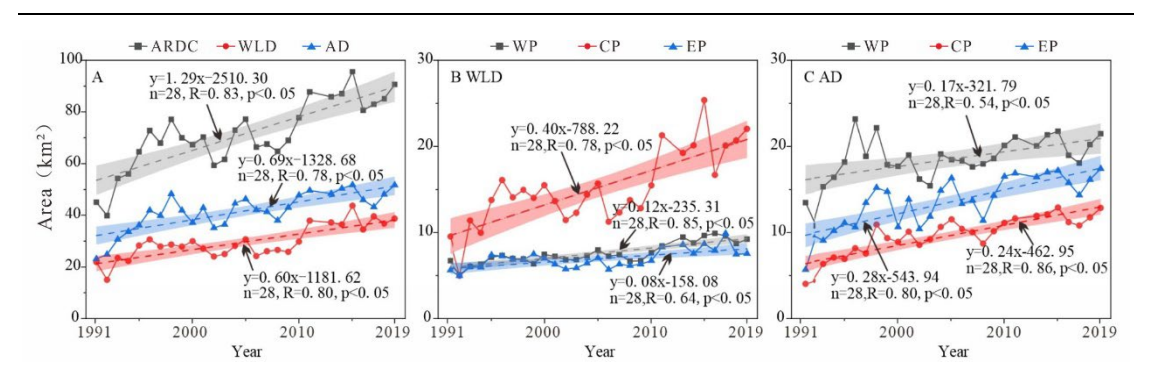


Figure 6. Temporal changes in deltaic island area

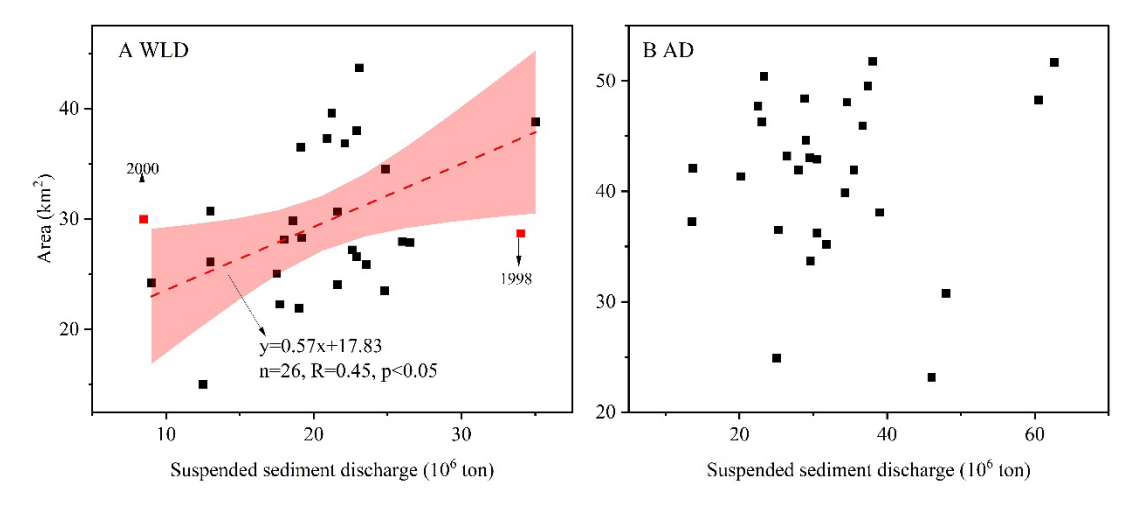


Figure 7. The relation of SSD and deltaic island area

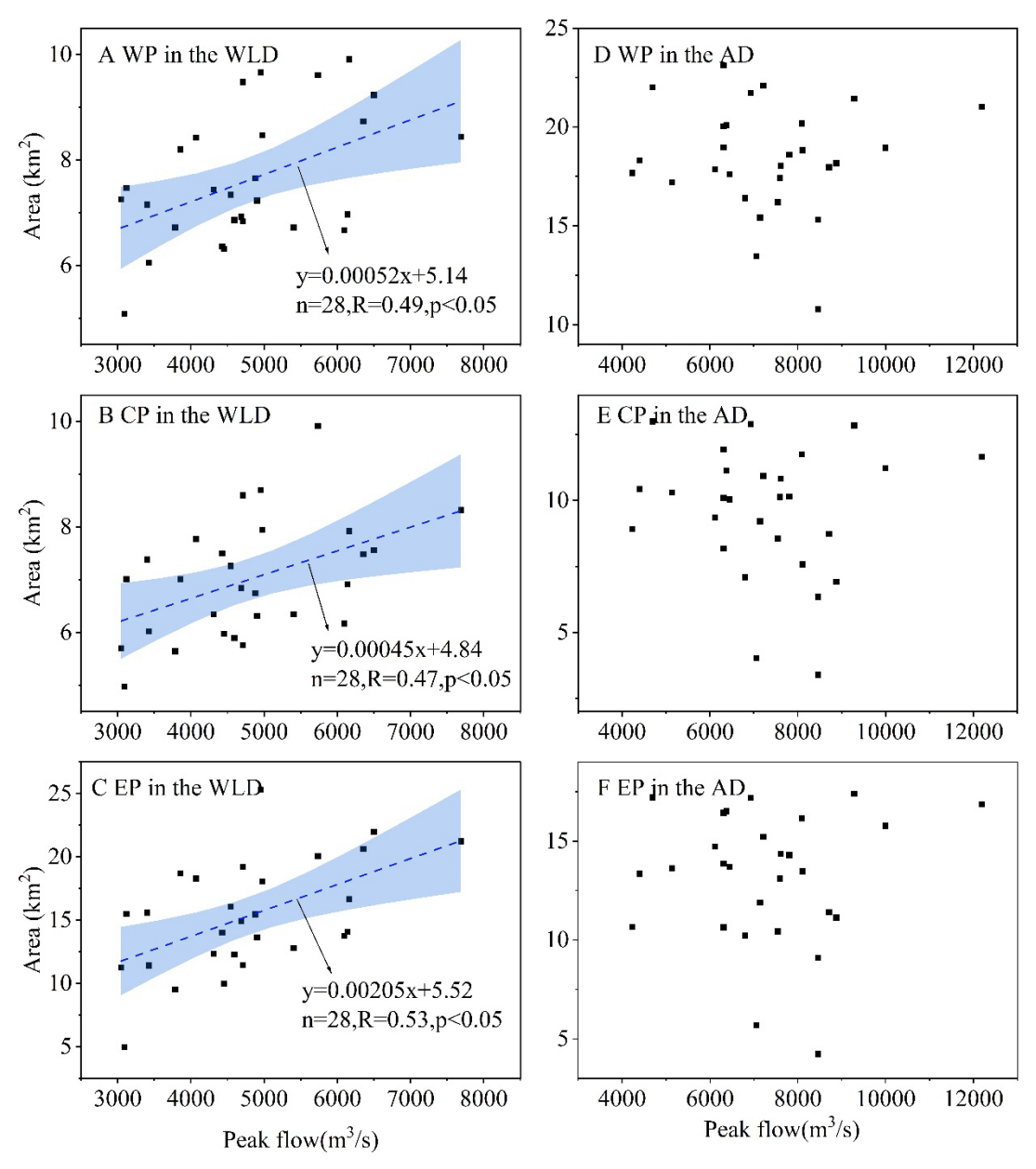


Figure 8. The relation between peak discharge and deltaic island area of each part

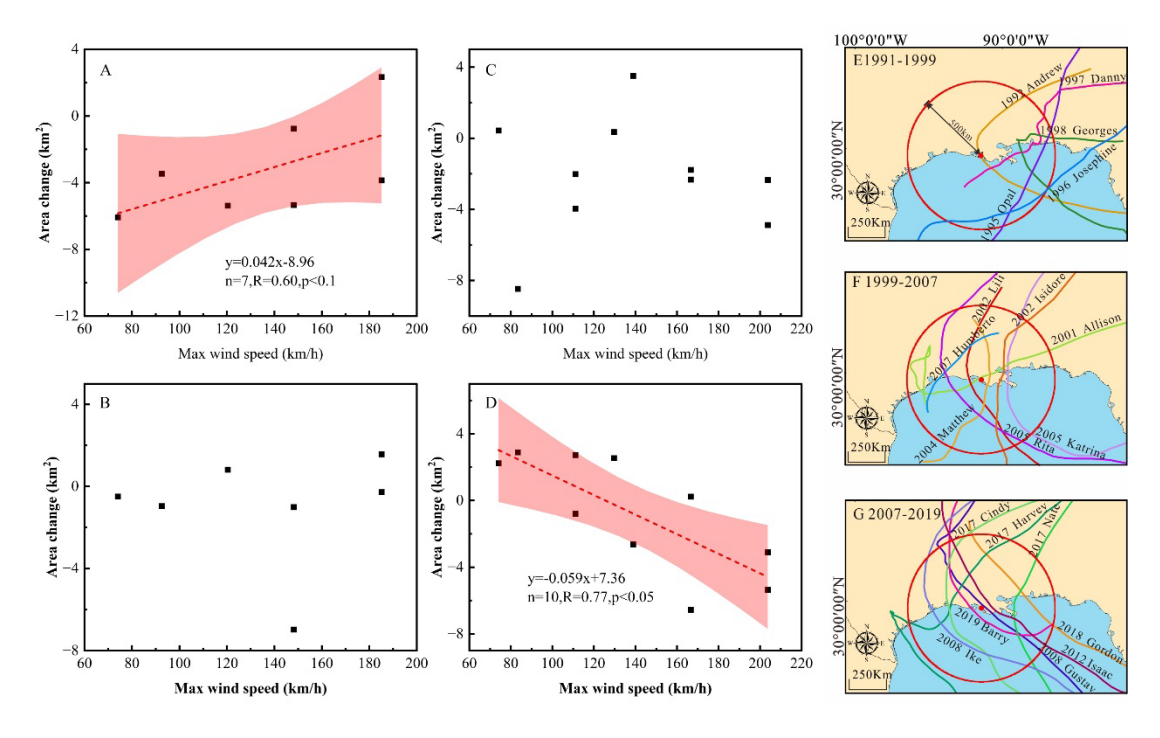


Figure 9. Relation between max storm wind speed of a tropical cyclone and area change of deltaic islands. A-B. Relation between max storm wind speed of a tropical cyclone landing west and east of the ARDC and area change of deltaic islands in WLD; C-D. Relation between max storm wind speed of a tropical cyclone landing west and east of the ARDC and area change of deltaic islands in AD; E-G. Hurricane and tropical storm tracks in 1991-1999, 1999-2007 and 2007-2019

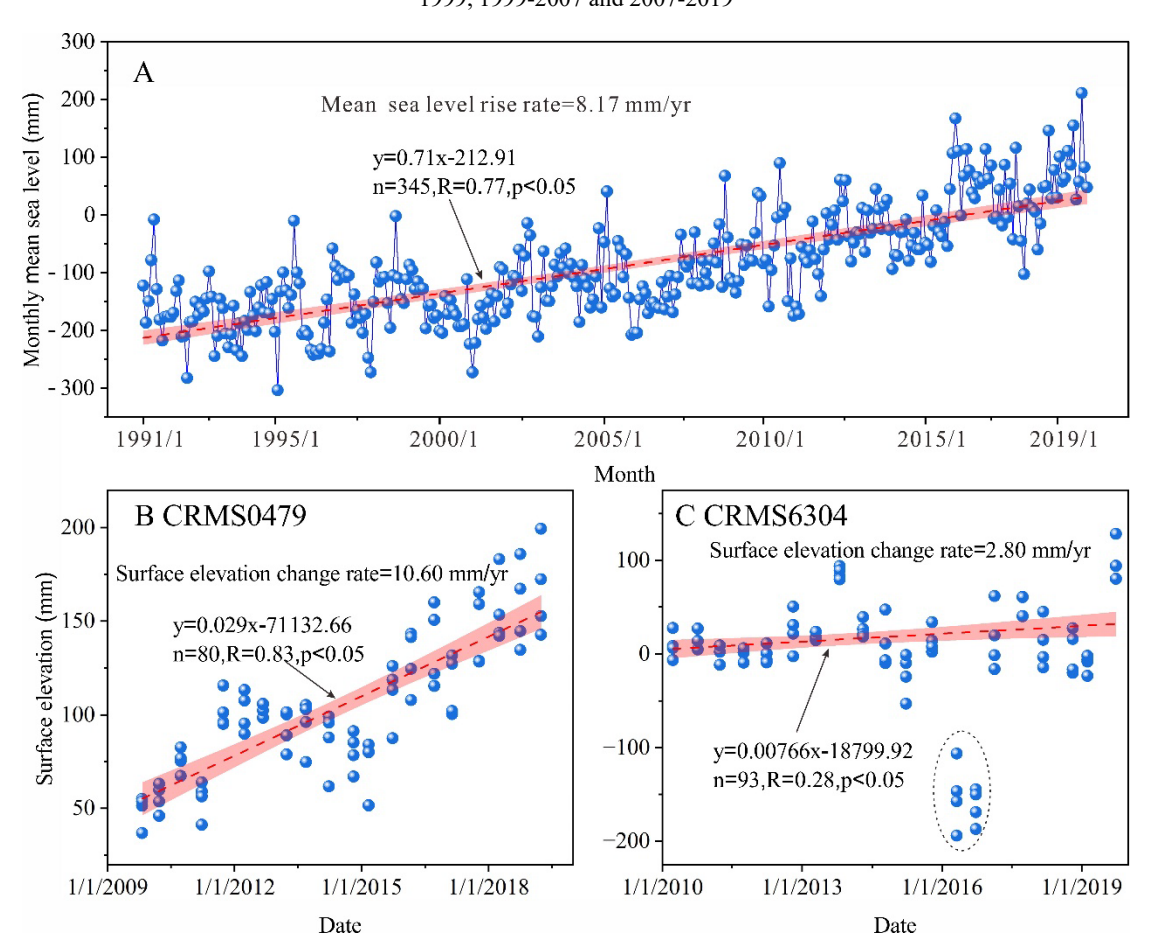


Figure 10. Sea level rise and deltaic island elevation change. A. Annual mean sea levels at the Grand Isle tidal station between 1991 and 2019; B. Surface elevation change measured at the CRMS0479 in the WLD; C. Surface elevation change measured at the CRMS6304 in the AD. The elevation of highlighted cluster in 2016 was significantly lower compared to the surrounding years, suggesting that these may be anomalous data, and they were excluded to prevent them from influencing the results of the correlation analysis

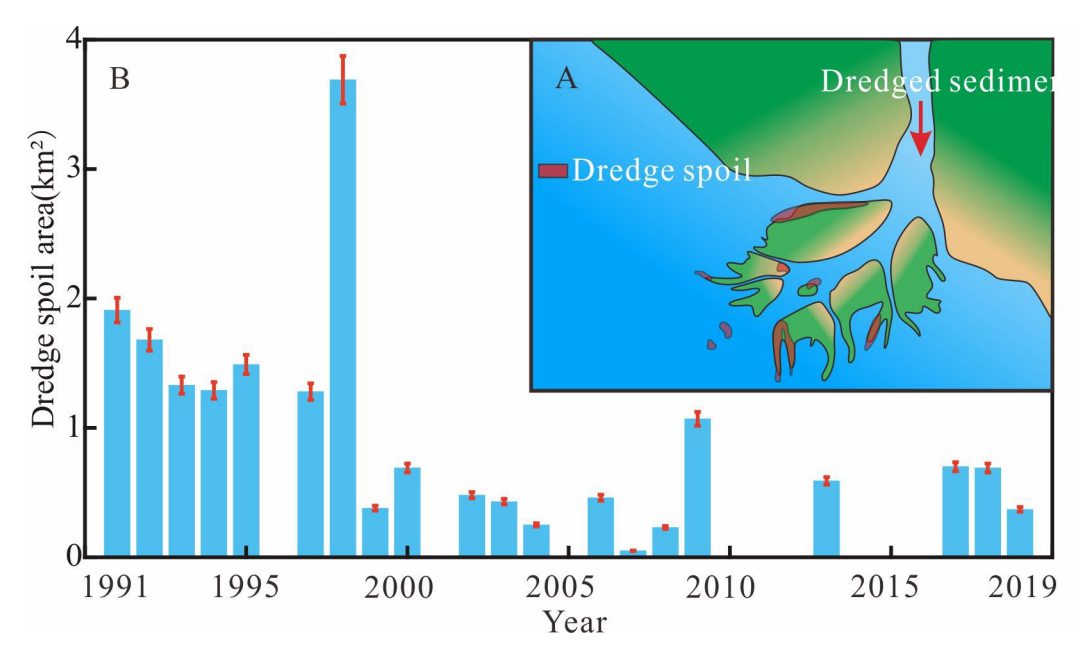
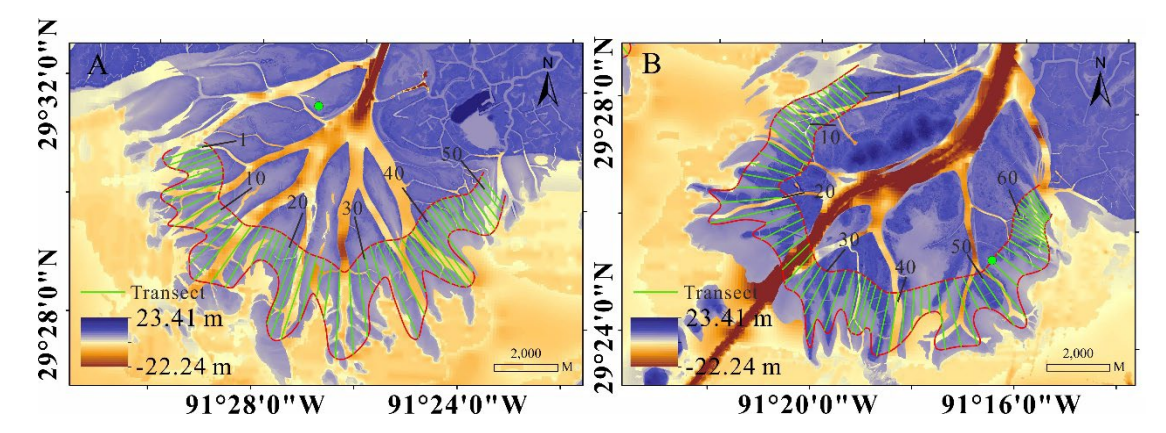


Figure 11. Deltaic lands formed by dredge spoils. A. Dredge spoil model. The red polygons indicated the newly formed deltaic lands due to the dredge spoils. B. Deltaic lands formed by dredge spoils in the AD from 1991 to 2019. Dredging spoil land area from 1991 to 2017 was collected by Zhang et al. (2021)



Auxiliary Fig. S1 The DEM map based on USGS Atchafalaya 2 Lidar. A. Transects in WLD; B. Transects in AD. Transects were selected about 200 m interval, extending 1 km from the shoreline in 2019 landwards



Auxiliary Fig. S2 Northwestern WLD in 2005/11. The image showed a few structures, houseboats and moorings in northwestern WLD

Table 1 Deltaic island area in the WLD corresponding to tide level at Grand Isle station, Overall accuracy and Kappa coefficient

Image time	Tide level (m)	Area (km²)	Overall accuracy	Kappa coefficient
1991-06-20	0.00	21.90	0.957	0.913
1992-09-10	0.35	15.02	0.956	0.963
1993-06-09	0.29	23.48	0.975	0.949
1994-08-15	0.22	22.27	0.967	0.986
1995-09-03	0.18	28.30	0.980	0.961
1996-07-03	0.16	30.67	0.942	0.933
1997-09-08	0.10	27.96	0.985	0.969
1998-07-09	0.12	28.70	0.933	0.942
1999-09-14	0.16	27.88	0.998	0.997
2000-09-16	0.16	29.97	0.965	0.921
2001-09-27	0.17	27.19	0.994	0.987
2001-03-27	0.25	24.06	0.958	0.932
2002-08-03	0.16	25.04	0.974	0.948
2003-07-07	0.14	28.14	0.974	0.925
2004-07-23	0.14	30.72	0.976	0.930
2005-08-13	0.16	24.22	0.992	0.899
2000-09-01	0.13	26.11	0.985	0.969
2007-09-20	0.13	26.59	0.983	0.973
2009-08-24	0.19	25.87	0.932	0.878
2010-09-28	0.19	29.85	0.939	0.913
2010-09-28	0.09	38.00	0.923	0.979
2011-08-30	0.16	37.30	0.943	0.925
2013-00-10	0.10	36.48	0.943	0.965
2014-09-23	0.16	43.68	0.989	0.979
2013-07-08	0.16	34.50	0.989	0.933
2010-09-28	0.33	34.30 39.59	0.935	0.933
2017-09-13	0.20	39.39 36.85	0.966	0.912
2018-09-18		38.78	0.985	0.924
2019-09-03	0.15	30./8	0.983	0.970